Spectral Profiles to Minerals Identification: An Integrated Hyperspectral vs Multispectral Minerals Exploration of the Ophiolitic Belt of Qilla Saifullah District, Baluchistan

Abdul Mohsin[1], Javed Iqbal[1], Junaid Aziz Khan[1], Abdul Jabbar Khan[1], Krystyna Michalowska[2]
[1]National University of Sciences & Technology, School of Civil and Environmental Engineering, Institute of Geographical Information System, H-12, Islamabad, Pakistan
[2]AGH University of Krakow Poland
*Correspondence: amohsin.ms23igis@student.nust.edu.pk

Citation | Mohsin. A, Iqbal. J, Khan. J. A Khan, A. J, Michalowska. K, "Spectral Profiles to Minerals Identification: An Integrated Hyperspectral vs Multispectral Minerals Exploration of Ophiolitic Belt of Qilla Saifullah Baluchistan", IJIST, Vol. 7 Issue. 4 pp 3227-3261, December 2025

Received| November 22, 2025 **Revised|** December 17, 2025 **Accepted|** December 19, 2025 **Published|** December 22, 2025.

Baluchistan, the largest province of Pakistan, hosts abundant metallic and non-metallic mineral resources, particularly copper, gold, chromite, lead-zinc, and rare earth elements, making it a strategic region for mineral exploration and geological characterization. Despite such potential, mineral exploration in the province's ophiolitic belts remains limited by sparse ground surveys, logistical challenges, and incomplete spatial coverage. To address this gap, the present study aimed to (1) Key ophiolitic minerals (chromite, serpentine, magnesite) and associated lithologies with high spectral precision, and (2) Compare hyperspectral and multispectral sensors for mineral identification and mapping. The methodology integrated ZiYuan-1 02D (ZY-1E) hyperspectral satellite data (spectral range 0.4–2.5 μm) with advanced spectral analysis techniques i.e. Diagnostic Absorption Feature extraction, Spectral Matching against the United States Geological Survey (USGS) Spectral Library, and multiple classifiers including Spectral Angle Mapper (SAM), Spectral Feature Fitting (SFF), Random Forest (RF), and targeted band ratios/indices. Mineral point data and lithological maps from the Geological Survey of Pakistan (GSP) were used for accuracy assessment. For comparative analysis, multispectral datasets from ASTER, Landsat-8 OLI, and Sentinel-2 MSI were processed, with a focus on the efficacy of SWIR coverage for mineral detection. Results indicated that ZY-1E hyperspectral data achieved 81.82% mineral classification accuracy and 86.11% lithology mapping accuracy, with Band Ratio techniques emerging as a rapid detection tool. Among multispectral datasets, ASTER outperformed Landsat-8 and Sentinel-2 due to its six SWIR bands, enabling superior discrimination of OH-, Al-, and carbonate-bearing minerals. The study concludes that hyperspectral imagery, due to its high spectral resolution, is indispensable for precise mapping of minerals and lithology in rugged, inaccessible terrains. However, ASTER remains a cost-effective alternative for targeted mapping of alteration minerals where hyperspectral coverage is unavailable. It is recommended to integrate hyperspectral mapping in strategic exploration campaigns to accelerate mineral resource assessment in underexplored regions of the world.

Keywords: Ophiolites, Hyperspectral, Multispectral, Diagnostic Absorption Features, Alteration Minerals, USGS Spectral Library.

Introduction:

At the time of independence of Pakistan back in August 1947, it was perceived that Pakistan lacks in mineral potential, despite having occurrences of large deposits of salt, gypsum, limestone, marble, etc [1] The geological community of Pakistan should be credited for the discovery of major gas fields in Baluchistan, uranium from the foothills of the Sulaiman Range in Punjab and southern Khyber Pakhtunkhwa (KP), barite from Baluchistan and KP, chromite and China clay in KP, famous emerald in KP, copper-gold and lead-zinc in Baluchistan and KP. Numerous studies have been conducted showing the potential of Pakistan's economic minerals [2], with abundant resources at various locations [3][4][5][6]. Moreover, recent studies and reports [7][8] present a comprehensive detail on the mineral potential of Pakistan. Additionally, province-wise minerals as well as basin details have also been updated [9].

Baluchistan is abundantly enriched with metallic as well as non-metallic resources, making it a focal point for multiple minerals, ranging from economic to Rare Earth Elements (REE) and precious metals [10][11][1]. The Baluchistan basin consists of Cretaceous to recent sediments, as well as metamorphic and igneous rocks. The first pioneering geological work in the Baluchistan Basin was done by [12] where mapping of the first ever sedimentary, igneous, and metamorphic rock units across large tracts; delineation of major fold-thrust belts and mélanges was performed. In lines with production report from Baluchistan during 2007-08 [13], 36,583 tons (t) copper, 245 t antimony, 49,268 t barite, 331 t basalt, 33,815 t chromite, 25t clay, 2,325,220 t coal, 291 t granite, 259 t rhyolite, 134 t diorite, 183 t gabbro, 2431 t serpentinite, 98 t gneiss, 323 t quartzite, 360 t Sulphur, 176 t dolomite, 424 t fluorite, 75 t galena, 15,808 t iron ore, 727,951 t limestone, 70,740 t marble (onyx), 267,312 t marble (ordinary), 790 t magnesite, 1385 t manganese, 5060 t pumice and 1,306,764 t shale have been reported. It is pertinent to mention that what has been found so far is still too small than what is expected to be discovered, which indeed is not too distant future [14].

Remote Sensing and Minerals Exploration:

A convenient and cost-effective approach for mineral deposits exploration is the use of remote sensing [15][16]. Lithological mapping, together with mineralized zone detection, has proven the benefits of remote sensing data [17][18][19][20][21]. The use of spatial data for tracing and analyzing lithological maps to recognize the geological characteristics associated with the target mineralization is the key step in the mineral exploration process [22]. Generated maps include a variety of features, including minor and major structures, alteration types, diagnostic minerals, and lithological units [23][24][25]. Several workers tested different remote sensing techniques on the Oman ophiolite (Abrams and Rothery, 1988), [26], ophiolites in Egypt [27] and ophiolites in the Yarlung suture zone in Tibet [28] using mainly Thematic Mapper data sets. Ninomiya (2002) [29] used ASTER (Advanced Spaceborne Thermal Emission and Reflection Radiometer) data to discriminate carbonate, mafic, and ultramafic rocks. But there is not a single good technique to map ophiolites, mainly because ophiolites consist of a wide range of lithologies. Moreover, secondary minerals produced in different climatic zones, along with variable amounts of vegetation, may cover the characteristic spectral signals of the rocks.

Geological Settings of Baluchistan:

Geologically, Baluchistan is dominated by accreted fragments of the Tethyan belt, comprising ophiolites, sedimentary basins, and magmatic arcs [30]. The Tethyan collision belt consists of the Mediterranean, the Middle East, the Himalayas, and Southeast Asia, and includes at least 20 'megacities' and hosts more than half of the world's population [31]. As described in Ref 1, the western Indus suture is a suture between the Baluchistan basin (a part of Tethys) and the Indus Basin (a part of Gondwana). The western Indus suture is jointed just east of the Baluchistan basin, which is the reason being described here. It includes the

ophiolitic mélanges and sedimentary Mesozoic and Cenozoic sedimentary sequences. The ultrabasic rocks consist of altered pyroxenite, serpentinized peridotite, and amorphous and sheared serpentinite. The rocks of intermediate compositions are diorite and gabbro. The gabbro is a dark green rock spotted with large crystals of white feldspar, which is kaolinized. Some types are pegmatitic and exhibit crystals up to 4 inches across of biotite and pyroxene.

Muslimbagh Ophiolite Complex consists mainly of serpentinized ultrabasic rocks that include saxoniter, dunite, and pyroxenite. It also consists of dolerite, gabbro, and diorite, but these seem to be slightly later phases. The age is Late Cretaceous-Early Paleocene [32][33][34].

Chromite was first reported by R. H. Nagell [35] and its mining was started in 1903 in the Khanozai area and extended to Muslimbagh in 1915. In the early twenties, mining started in the Sra Salwat area, 29 km south of Muslimbagh. The following deposits, like Muslimbagh chromite (Qila Saifullah District) and Wad, Sonaro, and Ornach chromite (Khuzdar District), are significant [36]. The Muslim bagh area chromite (Qila Saifullah District) extends from Gwal to Nisai, about 100 km. This region boasts the most extensive deposits in Pakistan.

Hyperspectral Imagery and Minerals Exploration:

Since the inception of hyperspectral technology towards identification and exploration of minerals back in 1985 [37][38] (e.g., Goetz and Srivastava, 1985; Kruse, 1988), numerous studies and research have been conducted along with field validations to extract the naturally occurring minerals most efficiently. Ahmad et al. (2025) [39] ZY1-02D hyperspectral satellite imagery, which offers moderate spectral and high spatial resolution to perform lithological mapping in the Kohat–Pothohar Plateau, located along Pakistan's Main Boundary Thrust (MBT). The study combined spectral indices, false color composites (FCC), principal component analysis (PCA), support vector machine (SVM) classification, and spatial–spectral transformer (SSTF) deep learning models to classify key lithological units. PCA significantly enhanced lithological discrimination by extracting the highest eigenvalues. The generated lithological maps, validated through field surveys and laboratory analyses (XRD, photomicrographs, spectral profiles), successfully identified limestone, gypsum, sandstone, clay, and conglomerates. SVM and SSTF classification methods achieved high accuracies of 89.7% and 92.1%, respectively, demonstrating strong reliability in matching mapped geological boundaries. The study highlights the effectiveness of ZY1-02D hyperspectral data combined with machine and deep learning approaches for accurate geological mapping, with direct applications in mineral, oil, gas, coal, and uranium exploration.

Tong et al. (2023) [40] demonstrated that hyperspectral remote sensing technology enables rapid extraction of alteration minerals and linear structures based on spectral characteristics. The study areas of Zhaojinggou and Hutoushan in Wuchuan County, Inner Mongolia, were selected. Using ZY-1-02D satellite hyperspectral data, alteration minerals and linear structures were extracted based on spectral analysis techniques. The spatial distribution characteristics of these features were analyzed. Eight alteration minerals (hematite, low-aluminum sericite, medium-aluminum sericite, lepidolite, biotite, chlorite, carbonate, and kaolinite) and 127 linear structures were extracted. These features were closely related to lithology, concentrated in specific geological units. Linear structures were distributed along tonal boundaries and linear anomalies. Six prospecting areas were delineated, four of which coincided with known ore veins, confirming the reliability of remote sensing for mineral exploration.

Saeid Asadzadeh et al. (2024) [40] demonstrated the enhanced mineral mapping potential of the Environmental Mapping and Analysis Program (EnMAP) satellite, which captures 224 contiguous spectral bands between 420–2450 nm at a 30-meter spatial resolution. Unlike conventional multispectral sensors (e.g., ASTER, Sentinel-2), which are limited by broad spectral bands, EnMAP's fine spectral sampling (8.1 nm in VNIR and 12.5 nm in SWIR) enables precise identification of mineral absorption features. The authors applied a polynomial

fitting technique to EnMAP's Level 2A data to extract diagnostic absorption parameters, including minimum wavelength, depth, width, and asymmetry for key alteration minerals in the Reko Diq porphyry Cu-Au deposit (Chagai Belt, Pakistan). This study successfully mapped white micas (2195–2210 nm), chlorite, epidote, calcite, kaolinite, gypsum, jarosite, and ferric/ferrous iron minerals, revealing distinct zonation patterns associated with mineralization. Notably, Al-rich white micas (shorter wavelengths) were found proximal to mineralized zones, while ferrous iron and chlorite-epidote-calcite assemblages marked potassic and propylitic alteration zones, respectively. The study underscored EnMAP's superiority over multispectral sensors in delineating alteration mineralogy, providing a robust tool for porphyry copper exploration in exposed terrains worldwide.

Mahboob et al. (2024) [41] demonstrated the efficacy of integrating satellite remote sensing data with ML algorithms, specifically Random Forest (RF), Support Vector Machine (SVM), and Convolutional Neural Networks (CNN), for predictive modeling of copper (Cu) deposits in Pakistan's North Waziristan region. The critical gap in mineral exploration, the underutilization of ML techniques in processing multi-parameter datasets, including hydrothermal alteration maps derived from satellite imagery and limited field data, is highlighted in the study. By developing nine predictor maps and evaluating model performance using confusion matrices, statistical measures, and ROC curves, they found that the RF algorithm outperformed SVM and CNN in predictive accuracy, consistency, and interpretability. Notably, the RF model successfully delineated high-potential zones that aligned with known Cu deposits, thereby validating its robustness for targeting exploration. Their prospectivity map, which classified regions into low to very-high potential zones, led to the discovery of a new deposit, hence underscoring the practical utility of their approach.

Jan et al. (2024) [42] proposed a hybrid 1-Dimensional CNN-SVM model for mineral classification using Sentinel-2 multispectral data, achieving a classification accuracy of 95.3% with a polynomial kernel degree of 12. Their study demonstrated that combining CNN-based feature extraction with SVM classification outperformed traditional methods such as ANN-Softmax (93.4% accuracy) and CNN-RF (94.01% accuracy) in delineating carbonate minerals, rocks, vegetation, water, and urban areas in Pakistan's MARDAN and BUNER regions. The hybrid model's success was attributed to SVM's ability to capture complex, non-linear relationships in high-dimensional spectral data, while CNN layers efficiently extracted discriminative features from 1D reflectance values. This work aligns with broader trends in mineral exploration where ML/DL hybrids are increasingly adopted to address limitations of conventional methods.

Anees et al. (2022) [43] demonstrated the efficacy of integrating ASTER (multispectral) and Hyperion (hyperspectral) data in mapping lithological units and identifying mineralized zones in Chitral, NW Pakistan. This study employed band ratios, spectral indices (e.g., calcite, dolomite, hydroxyl, ferrous), principal component analysis (PCA), and spectral angle mapper (SAM) to discriminate rock types and alteration minerals. ASTER's superior spectral resolution enabled mapping of carbonates and granites, while Landsat-8's radiometric strength distinguished metamorphic rocks. Hyperion's hyperspectral data identified alteration minerals such as montmorillonite, muscovite, and pyrite, pinpointing potential mineralization zones in the Drosh-Shishi Valley. The study highlighted the complementary strengths of multi-sensor data, with ASTER excelling in carbonate detection and Hyperion in alteration mineral mapping, despite challenges like topographic noise and spectral mixing.

Lobo et al. (2021) [44] evaluated the effectiveness of HSI combined with ML classifiers, Linear Discriminant Analysis (LDA), Support Vector Machines (SVM), and Random Forest (RF) for distinguishing key minerals (e.g., cassiterite, wolframite, chalcopyrite) in tin–tungsten deposits. Their study compared two imaging scenarios: (1) laboratory-based HSI under controlled conditions and (2) a simulated mine face scan replicating field

conditions. Key findings include: Laboratory HSI achieved 98% classification accuracy, underscoring the precision of hyperspectral data under ideal conditions. Performance declined slightly when analyzing spectral ranges (450–950 nm and 950–1650 nm) independently and dropped significantly (74.5% accuracy) for conventional RGB imagery, thereby highlighting the limitations of broadband sensors. In the simulated mine face scan, accuracy remained high (85%), though reduced spatial resolution and field-like conditions introduced challenges, particularly in distinguishing cassiterite from wolframite (70% user accuracy). Random Forest (RF) marginally outperformed LDA and SVM in classification robustness, with a lumped ore category achieving 94.9% user accuracy, demonstrating practical utility for ore mapping.

Khan et al. (2018) [45] highlight the evolution of HSI over three decades, emphasizing its enhanced spatial, spectral, and temporal resolutions that enable precise identification of materials with visually similar but spectrally distinct signatures. The review categorizes modern HSI applications into: (1) food quality/safety inspection, where it detects contaminants and chemical composition; (2) medical diagnostics, including surgical guidance and disease detection; (3) forensic science, particularly document forgery detection; (4) defense/security for threat identification; and (5) remote sensing applications like precision agriculture and water resource management. Notably, the authors underscore the growing role of deep learning in advancing HSI analysis, particularly for complex tasks such as forgery detection in questioned documents. This synthesis aligns with broader trends in HSI research. The review also identifies gaps, such as the need for real-time processing algorithms and miniaturized HSI systems for field deployment, suggesting directions for future research.

Ahmad et al. (2025) (as shown in Ref. 42) leveraged ZY1-02D hyperspectral data (with high spatial resolution) combined with machine learning (SVM) and deep learning (SSTF) methods to achieve exceptional lithological classification accuracy (89.7% for SVM, 92.1% for SSTF). The methodology integrated spectral indices, PCA, and field-validated techniques (XRD, photomicrographs) to discriminate limestone, gypsum, sandstone, and conglomerate units critical for hydrocarbon and mineral exploration near the Main Boundary Thrust. This work builds on foundational HSI applications in geology while advancing the field in three key ways: 1. Sensor Innovation: First demonstrated application of China's ZY1-02D satellite data for lithological mapping, showcasing its superior spatial-spectral capabilities. 2. Algorithm Comparison: Quantitative validation of SSTF's superiority (92.1% accuracy) over traditional SVM for geological classification 3. Exploration Utility: Direct linkage between mapped units and economic deposits (oil, gas, gypsum), bridging academic research and industry needs. The study further suggests integration with geophysical data for 3D reservoir modeling, Extension to other tectonic regions with complex stratigraphy, and Real-time processing pipelines for exploration campaigns.

Giri et al. (2024) [46] used AVIRIS-NG data from Jahazpur, Rajasthan, developing a stacked ensemble learning framework combining multiple base learners (Naïve Bayes, KNN, ANN, Decision Tree, SVM) with a Random Forest meta-learner, achieving exceptional performance metrics (98.96% overall accuracy, 0.9628 Kappa coefficient) for mapping key minerals including talc, montmorillonite, and kaolinite. This work makes three significant contributions to the field: 1. Algorithm Innovation by introducing a novel stacked ensemble approach that outperforms individual ML models in mineral classification, 2. Application Precision, which demonstrates AVIRIS-NG's capability for discriminating between spectrally similar phyllosilicate minerals, 3. Methodological Rigor to establish a replicable framework for mineral mapping with quantified accuracy metrics.

Islam et al. (2024) [47] utilized ASTER multispectral data and employed an integrated approach that combined FCC, PCA, Decorrelation Stretch, and machine learning (TRTC) to successfully map lithological units and identify five new mineralization targets associated with copper and iron deposits. Their methodology achieved precise discrimination of alteration

minerals (chlorite, limonite, muscovite) and validated findings through field campaigns, XRD analysis, and spectral measurements. This work significantly advances previous studies in three key aspects: Methodological Integration: Combines traditional image processing (PCA, FCC) with modern ML techniques (TRTC) for enhanced lithological discrimination Exploration Breakthroughs: Identifies new mineralization zones in Shishi, Maroi and Drunil valleys - expanding known mineral potential in collisional belts Validation Protocol: Establishes rigorous ground truthing through petrography, XRD and spectral analysis. The study builds upon foundational work in ASTER applications (Ninomiya & Fu, 2003), [48] while addressing critical gaps in: High-relief terrain mapping challenges, Phyllosilicate mineral discrimination, Metallogenic potential assessment in orogenic belts. Future research directions include: Integration with hyperspectral data for improved alteration mapping.

Bedini (2017) [49] provides a seminal and comprehensive review of hyperspectral remote sensing applications in mineral exploration, systematically evaluating three decades of technological advancements and their practical implementation across diverse deposit types. The study categorizes ore deposits by genetic processes (magmatic, hydrothermal, sedimentary, supergene). It assesses hyperspectral effectiveness for each, establishing critical benchmarks for proven applications, documents successful case studies for Kimberlite/ carbonatite diamond/REE exploration, Hydrothermal deposits (porphyry, epithermal, VHMS), Sedimentary-exhalative (SEDEX) Pb-Zn-Ag systems, underexplored potentials, identifies key gaps for Ni-sulfide deposits in mafic/ultramafic rocks, Sedimentary uranium and MVT Pb-Zn deposits, Lateritic bauxite and banded iron formations, technology assessment, contrasts capabilities of airborne vs. spaceborne systems, VNIR-SWIR vs. emerging thermal infrared sensors, Spatial resolution requirements for deposit-scale mapping, etc. This work builds upon foundational hyperspectral principles while providing the first systematic framework for matching sensor capabilities to deposit types, optimizing spatial/spectral resolution tradeoffs. Integrating hyperspectral data with exploration workflows.

Novelty of the Study:

Maiden application of ZY-1E hyperspectral imagery for mineral and lithological mapping of underexplored ophiolitic belts of Baluchistan. Previously, no such study in Pakistan has utilized full-range (0.4–2.5 μm) of satellite based hyperspectral data and made use of diagnostic absorption features of chromite, serpentine, and magnesite within ophiolitic collections. Further, direct, quantitative comparison of hyperspectral and multispectral sensors (ASTER, Landsat-8 OLI, Sentinel-2 MSI) under identical geological and validation conditions allowed us to isolate the role of spectral resolution, particularly the SWIR region, for minerals discrimination. Unlike earlier research, which only relied on multispectral indices or visual interpretation, this research integrates diagnostic absorption feature extraction, USGS spectral library matching, physics-based classifiers (SAM and SFF), machine-learning classification (Random Forest), and targeted band ratios within a single, unified framework. Notwithstanding, a rigorous accuracy assessment strategy using known mineral occurrence point data and lithological maps from the Geological Survey of Pakistan (GSP), providing statistically defensible validation rarely reported in regional ophiolite studies, is also explained. Study reveals that ZY1E hyperspectral data achieves substantially higher mineral and lithological mapping accuracies than multispectral sensors in rugged and inaccessible terrains, thereby making hyperspectral satellite imagery an operational exploration tool rather than an experimental approach.

Materials and Methods:

Study Area:

The diverse geology of the Qilla Saifullah district gives rise to a variety of mineral resources, where deposits of chromite are well known with the Muslim Bagh ophiolites together with several other minerals of economic interest. Currently, chromite and magnesite

are actively mined in the district, while other minerals are present as prospects or small occurrences [50][51]. Potential minerals include Chromite, Magnesite, Manganese, Asbestos, and Calcite.

The Muslim Bagh ophiolite (earlier called Hindu Bagh) is located in the Zhob Valley northeast of Quetta and is one of the well-exposed ophiolites of Pakistan. The closure of the Neo-Tethys finally ended with the collision of the Indian plate with the Asian, Afghan, and Luth-continental blocks, which is dated at approximately 40 Ma ago [52]. The Muslim Bagh ophiolite was first reported on maps by Vredenburg (1901), [53]. The Muslim Bagh ophiolite comprises two main bodies known as Jang Tor Ghar (JTG) and Saplai Tor Ghar (STG). These two bodies are structurally related and belong to the same ophiolite nappe and overlay a zone of subophiolitic "melange" and Mesozoic sediments (Hunting Survey Corporation Ltd., 1960) [12]. The Jang Tor Ghar massif consists of partially serpentinized peridotites (harzburgite and dunite) and covers an area of about 150 km2. The best preserved series of sub-ophiolitic metamorphic rocks is located at the north-western side of the Jang Tor Ghar massif [30].

The Eastern Block (Saplai Tor Ghar) has an area of about 600 sq km, showing nearly a complete ophiolitic sequence, as defined by the Penrose Conference (1972) [54]. Only the uppermost unit consisting of extrusive rocks and related sediments is missing. The metamorphic sole below the Saplai Tor Ghar block is lithologically similar to Jang Tor Ghar, though less complete, and is tectonically sheared off at the top and at the base of the sequence [55][56].

In the Muslim Bagh ophiolites, the mantle-crust transition section ranges in thickness from several meters to over one kilometer. It is composed of dunites, chromites, wehrlites, and troctolites containing pyroxenites and/or gabbros as discontinuous bands or lenses [57][58]. The study area map of our research is shown in Figure 1.

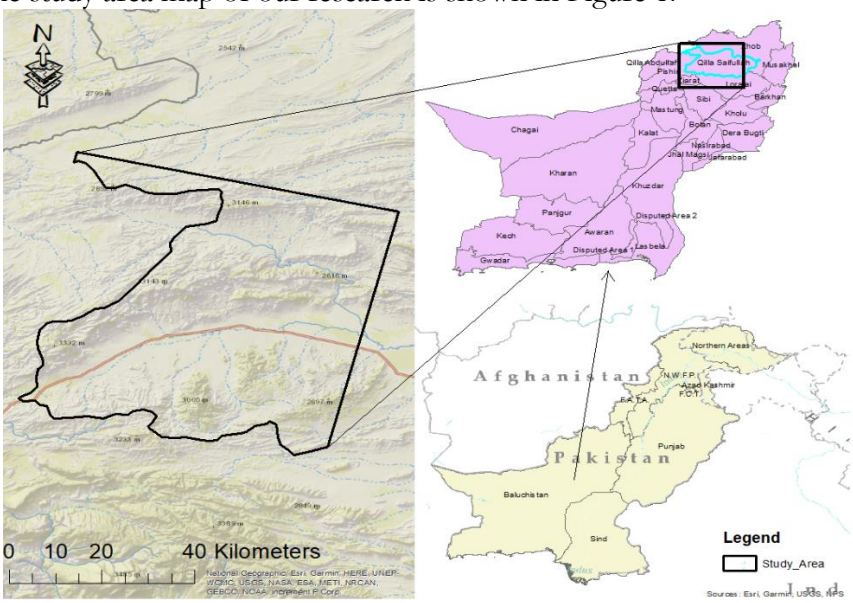

Figure 1. Study area map of research.

Datasets and Software:

Multiple datasets, including hyperspectral to multispectral imagery, USGS spectral libraries, minerals point data for validation/ ground truthing, and the geological maps of the Geological Survey of Pakistan (GSP), were used. In contrast, software including ArcMap, ENVI, and open-source Google Colab for Python coding were also utilized for the identification of minerals and lithological mapping. To ensure quick analysis by leveraging available computing resources and avoiding unnecessary data processing, not only were the unwanted/ bad bands from the hyperspectral dataset eliminated, but also the unnecessary

bands of multispectral sensors were removed to limit our analysis to minerals detection only. Time of datasets acquisition also plays an important role in avoiding unwanted cloud cover and capturing the imagery covering maximum details [58][59]. Considering the fact that our primary dataset for minerals extraction and lithological mapping was hyperspectral, concerted efforts were made to acquire multispectral datasets on the same date and time. However, acquisition of similar data and time imagery of some sensors could not be materialized due to no coverage during that desired timeframe. It is worth mentioning that old imagery of ASTER was acquired due to the issuance of NASA advisory/ alert [60] that says ASTER SWIR detectors got defect since April 2008, and despite rigorous efforts, faults could not be rectified; therefore, data acquired after April 2008 for ASTER SWIR sensors are not reliable. Hence, a dataset of old date i.e May 2007, was acquired for ASTER. Details of data acquisition dates, level of processing performed by the service provider, and details of bands being used are shown in Table 1. Whereas collective details of all required datasets and their sources are summarized in Table 2.

Methodology:

A step-by-step comprehensive methodology spanning over data acquisition, preprocessing, end member extraction, analysis, and finally accuracy assessment was formulated (Figure 2). Primarily, the methodology consists of these steps i.e. (1) Data acquisition including geological map of Baluchistan and field samples data of minerals in the form of point data from Geological Survey of Pakistan (2) Data preprocessing (3) Images stacking (VNIR and SWIR) (4) Endmember Extraction through Minimum Noise Fraction Transformation (MNFT), Pixel Purity Index (PPI) and n-Dimension Visualization. (5) Collection of diagnostic absorption features of expected minerals in our study area (6) Spectral Matching with USGS library (7) Minerals identification & Lithological Zoning based on alteration zones (8) Accuracy assessment and (9) Formulation of maps for minerals and lithologies. Details of the datasets acquisition are already explained in para 2.2, whereas a brief description of the relevant steps being followed is described in the ensuing paragraphs.

Table 1. Datasets acquisition dates, processing levels, and bands details.

Satellites	Acquisition Date	Processing level	Useful Bands	Removed Bands
ZY1E	30 Jul 2020	1A	140 (Total bands 166)	VNIR: 63 – 76 SWIR: 20 – 25 & Bands 50 – 55
ASTER	22 May 2007	1T	All 14 bands were used	The old dataset of ASTER is used due to the introduction of a defect in the SWIR sensor since April 2008. No bands were removed
Sentinel-2	30 Jul 2020	2A	10 bands were used, 08 VNIR & 02 SWIR	
Landsat-8	20 Jul 2020	2SP	07 bands were used, 5 VNIR & 2 SWIR	

Table 2. Summary of all datasets being used and their sources.

Data Type	Description	Source
Satellite Imagery		
ZY1E Hyperspectral	ZY1E Hyperspectral	ZY1E Hyperspectral
ASTER	ASTER	ASTER
Sentinel-2 (A, B)	Sentinel-2 (A, B)	Sentinel-2 (A, B)

Landsat-8	Landsat-8	Landsat-8
Spectral Reference Data		
USGS Spectral Library	USGS Spectral Library	USGS Spectral Library
Geological Maps	Geological Maps	Geological Maps
Field Validation Data	Field Validation Data	Field Validation Data
Software & Tools	Software & Tools	Software & Tools

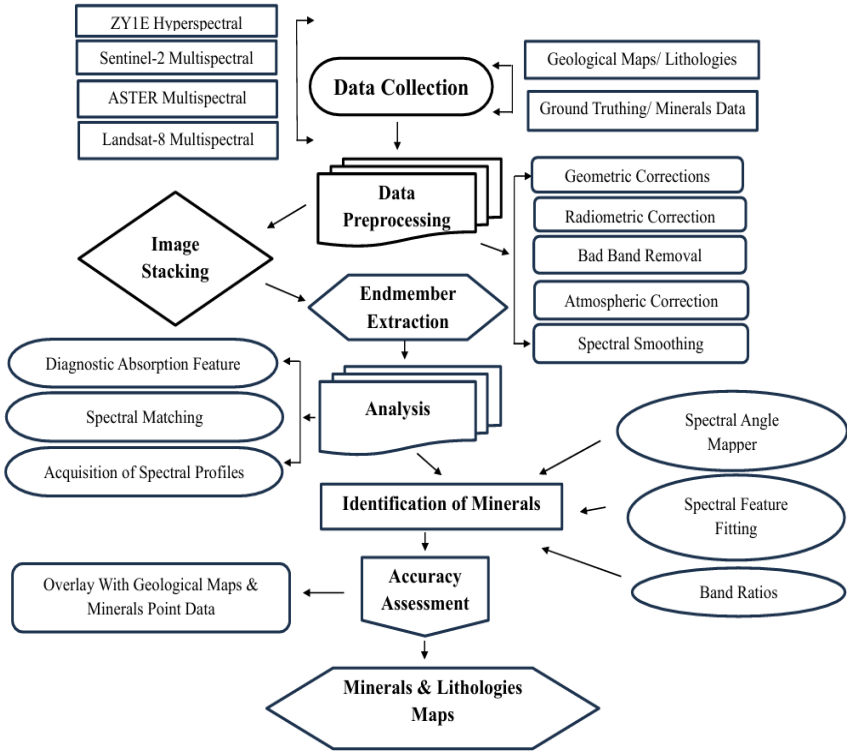

Figure 2. The complete methodology flowchart used in the study/ research.

Data Preprocessing:

Data pre-processing is the fundamental step or heart of Remote Sensing before the commencement of any analysis [61][62][63]. Here, satellite-observed raw Digital Number (DN) values are converted into meaningful units such as radiance or reflectance, thereby enabling accurate quantitative analysis and comparison for mineral identification. Pre-processing steps include:

Geometric Corrections: to rectify spatial distortions in raw imagery and ensure that all features are accurately georeferenced and align with real-world coordinates for precise mapping and analysis [64][65]. Geometric corrections details include Projection: UTM, Zone: 42 N, Units: Meters, Datum: WGS 1984, and Spatial Resolution: 30m.

Radiometric Corrections: Radiometric error is influenced by sensor calibration, sun illumination, and atmospheric interference. Therefore, in order to extract distinct spectral absorption and reflection features of specific minerals, radiometric correction is performed, which transforms the raw Digital Number (DN) values into accurate radiance values [66][67][68].

Atmospheric Corrections: To remove the scattering and absorption effects of atmospheric gases and aerosols and accurately represent the true reflectance properties of the Earth's surface [69][70][71][72]. In Envi, 02 x Tools exist for Atmospheric Corrections, i.e., QUAC [73][74] and FLAASH [75][76]. QUAC, an empirical in-scene atmospheric correction, was run on all images for atmospheric corrections.

Bad Bands Removal: Bad bands are spectral bands that contain little or no useful information amid severe atmospheric absorption (e.g., water absorption bands) or sensor

malfunctions [77][78][79]. Such bands are removed to prevent the introduction of noise or erroneous details. These bands could include overlapping bands as well. Accordingly, these bands are removed before further analysis. Multispectral datasets do not need this step due to limited spectral coverage. Figure 3 shows the details of the preprocessing steps.

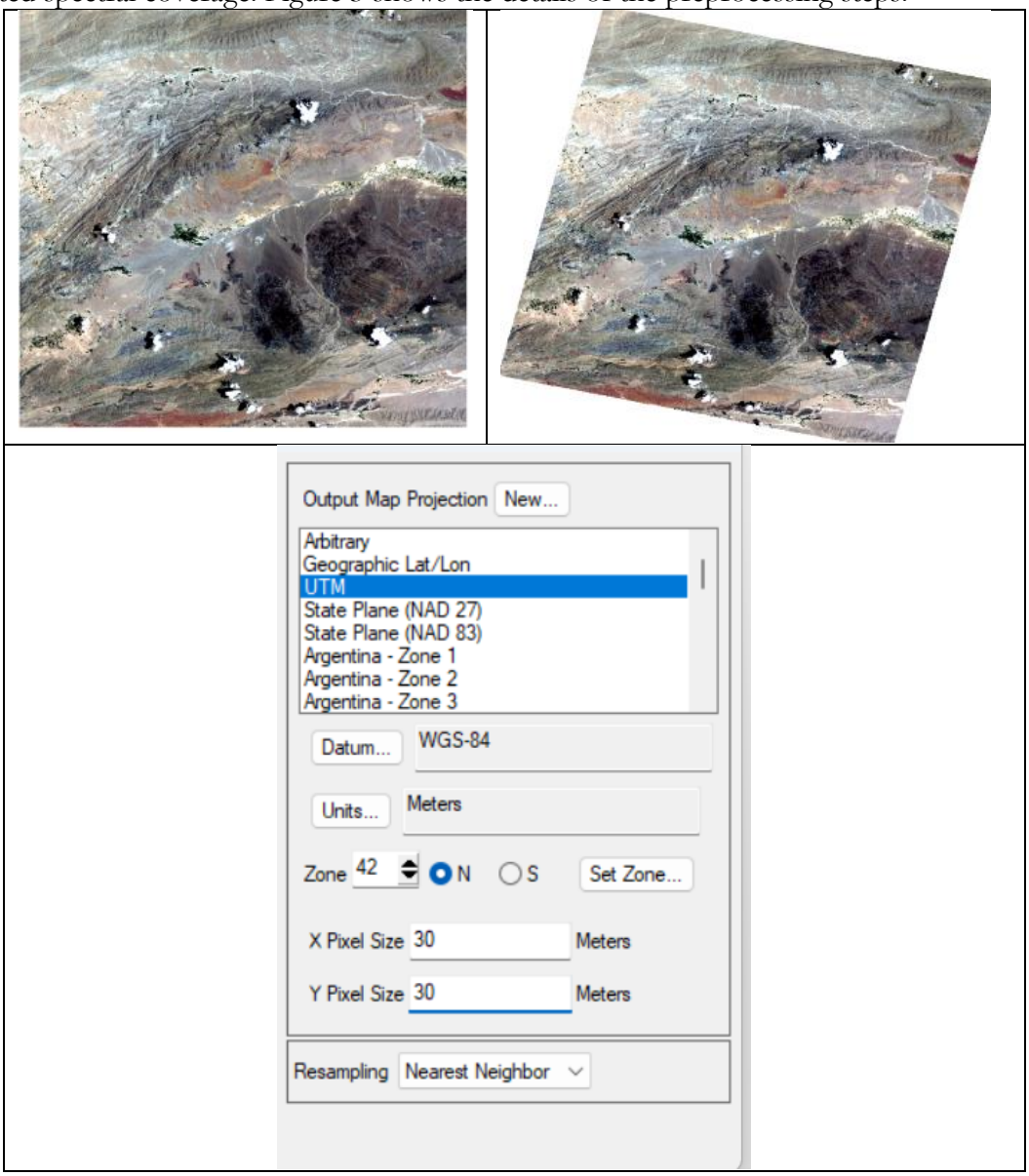

(a)

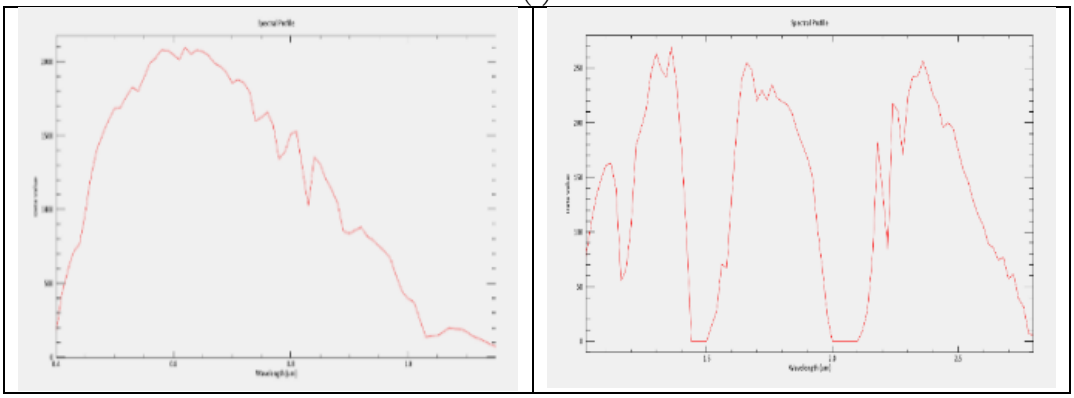

(b)

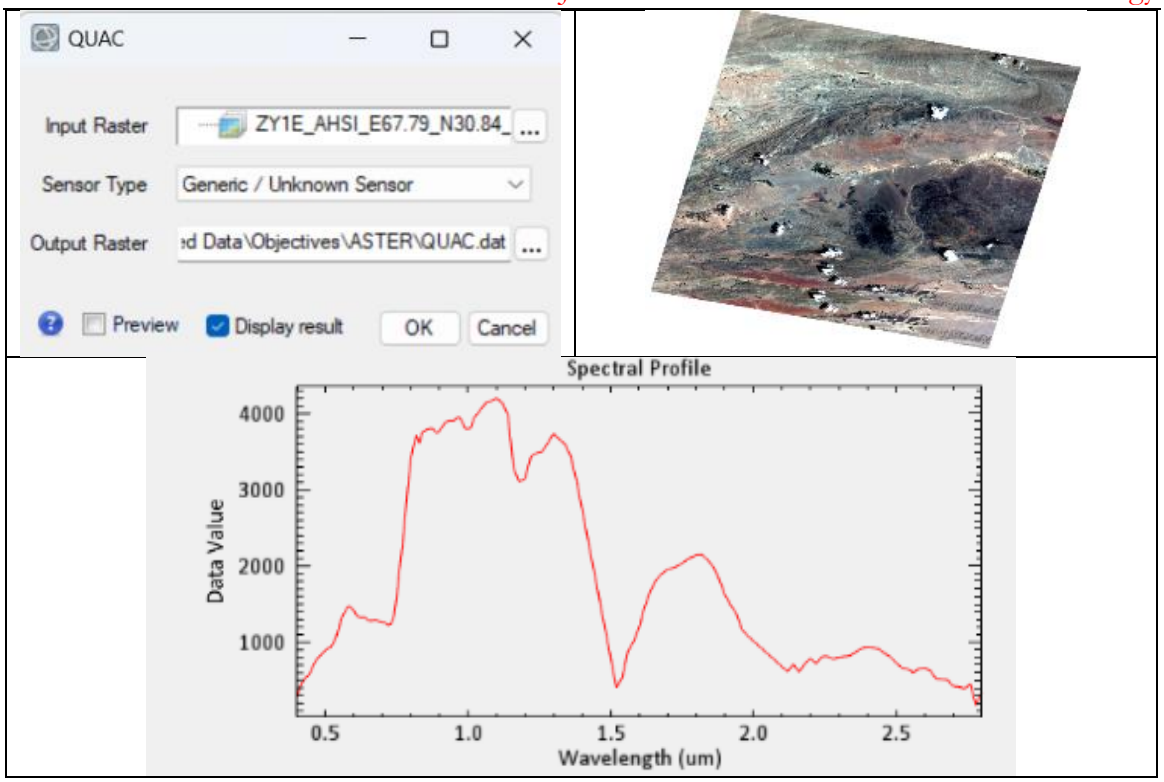

(c)

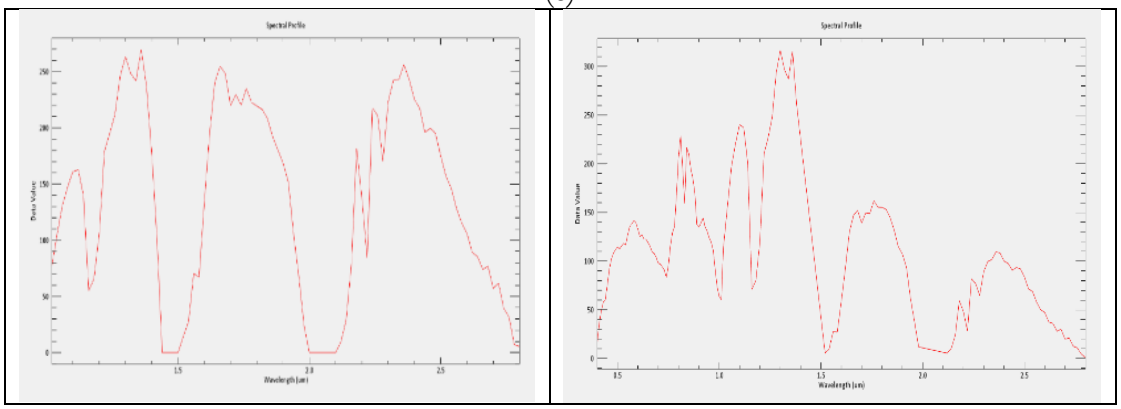

(d)

Figure 3. Data preprocessing steps (a) Image georeferencing, projection, and spatial resolution details, (b) Radiometric corrections showing spectral profile transformation, (c) QUAC Atmospheric corrections with spectral profile of vegetation pixel, (d) Removal of water absorption/ band bands.

Image Stacking:

An essential preprocessing step in multispectral and hyperspectral analysis, which allows spectral signatures to be analyzed across all wavelengths simultaneously by combining multiple single-band images into a single, multi-layered file, creating a composite dataset essential for integrated analysis, visualization, and the application of multi-spectral techniques [80][81] (Ref. 66, 68, 73, and 86 are also relevant). Both hyperspectral and multispectral bands were combined after pre-processing (Figure 4) to get a single composite imagery for subsequent detailed analysis.

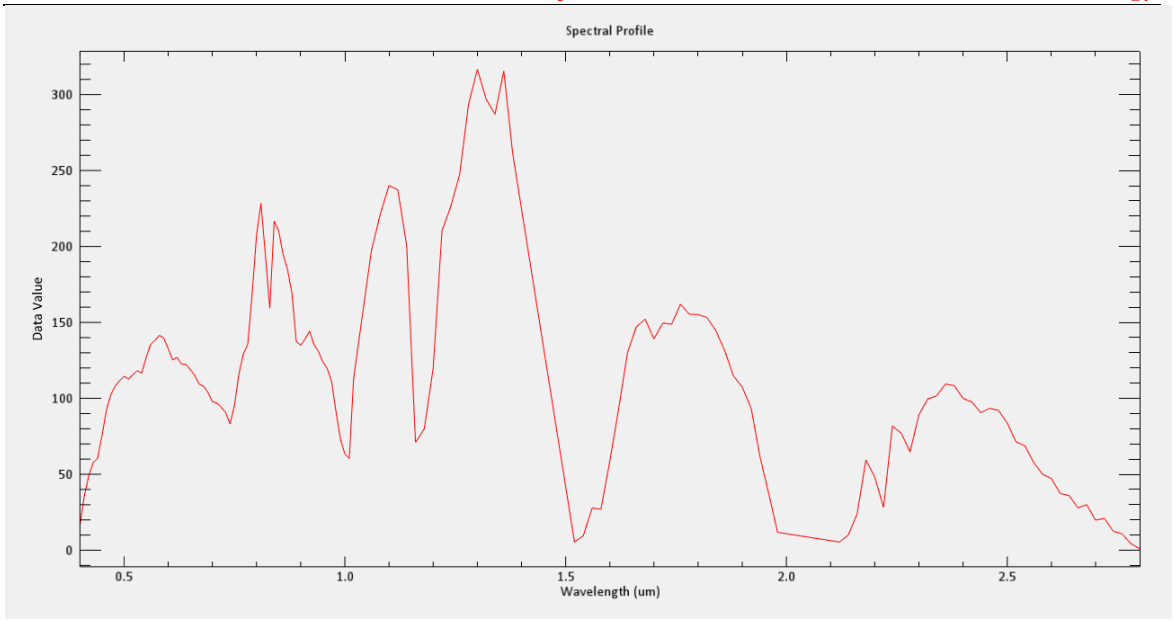

Figure 4. Spectral profile of vegetation pixel after stacking VNIR & SWIR images.

End Member Extraction:

Endmember extraction is a process of identifying the pure spectral signatures of materials from hyperspectral or multispectral imagery [82][83][84][85]. It is something like finding the ingredient colors in a mixed-color pixel and, hence, helping to map specific materials across an image. For end members extraction, we followed these 3 steps: 1. Minimum Noise Fraction Transformation (MNFT) 2. Pixel Purity Index (PPI) 3. N-Dimensional Visualization. MNF Transformation is the initial step that is applied to reduce data dimensionality and separate noise from the spectral signal [86][83]. It orders the bands by signal-to-noise ratio, i.e., effectively concentrating the spectral information into a few clean MNF bands. MNF curve plots data values, i.e., variance or eigenvalues, on the Y-axis against component index/ band index on the X-axis. It is a diagnostic output from the MNF transformation and is commonly used in hyperspectral image processing. The first few components i.e left side of the curve, have high variance and contain most of the signal/ information. Components with low variance, dominated by noise, are subsequently highlighted on the right side, which highlights the most informative and noisy band details. In hyperspectral image processing, the MNF curve helps to reduce dimensionality [80] by keeping only the most informative bands and suppressing noise by removing components having minimal signal [87]. Consequent upon completion of MNF, Pixel Purity Index (PPI) is performed on MNF output to identify the spectrally most extreme pixels in the transformed data, i.e., highly uncorrelated, which are strong candidates for pure endmembers. PPI iteratively projects n-Dimensional data onto random unit vectors and counts how many times each pixel falls/ moves at the extreme ends of these projections (same as Ref. 96). Those pixels that are consistently at extreme ends are considered as pure pixels and are therefore flagged as potential endmembers [88]. Hence, representing the distinct mineral spectra in our study area. A total of 10,000 iterations is run to get the purest signals. Accordingly, it is evident that after 10,000 iterations, the curve starts to flatten, i.e., no more distinct pure pixels exist afterwards [89].

Subsequent to MNF and PPI, n-Dimensional Visualization is performed as part of end members extraction. It is an interactive environment to visually analyze the pure pixels identified by PPI and select the conclusive endmembers [90][91]. It allows you to plot the MNF-transformed data in a multi-dimensional scatterplot, where each axis represents an MNF band. We selected a 3-dimensional axis for the selection of pixels. Accordingly, the most

extreme pixels carrying maximum information and no noise are selected as new classes in ENVI. Extreme pixels highlighted in red indicate the selected purest pixels. Details of the steps are shown in Figure 5.

It is pertinent to note that multiple studies validate that this visualization technique allows to rotate and exploring the data cloud, identifying clusters of spectrally similar pure pixels and manually selecting the most representative endmember spectra for your target minerals, thereby ensuring accuracy for mapping of minerals and their lithologies. Therefore, using the same principle and step-by-step procedure, spectra of all sensors were collected. i.e hyperspectral as well as multispectral.

Diagnostic Absorption Features:

Diagnostic absorption features are unique/ wavelength-specific dips in the reflectance spectrum of different materials that act as fingerprints, i.e., a primary source for identifying minerals using hyperspectral remote sensing data [92]. These specific dips or fingerprints arise from the unique ways electromagnetic radiations interact with the atomic and molecular bonds within a material [93]. Precise position, depth, width, and unique shape represent specific minerals or chemical compounds. For example, Serpentine shows a weak dip at 1400 nm and strong absorption features between 2300 and 2320 nm, which help to identify these minerals. A detailed summary of diagnostic absorption features of all expected minerals of our study area is placed in Table 3.

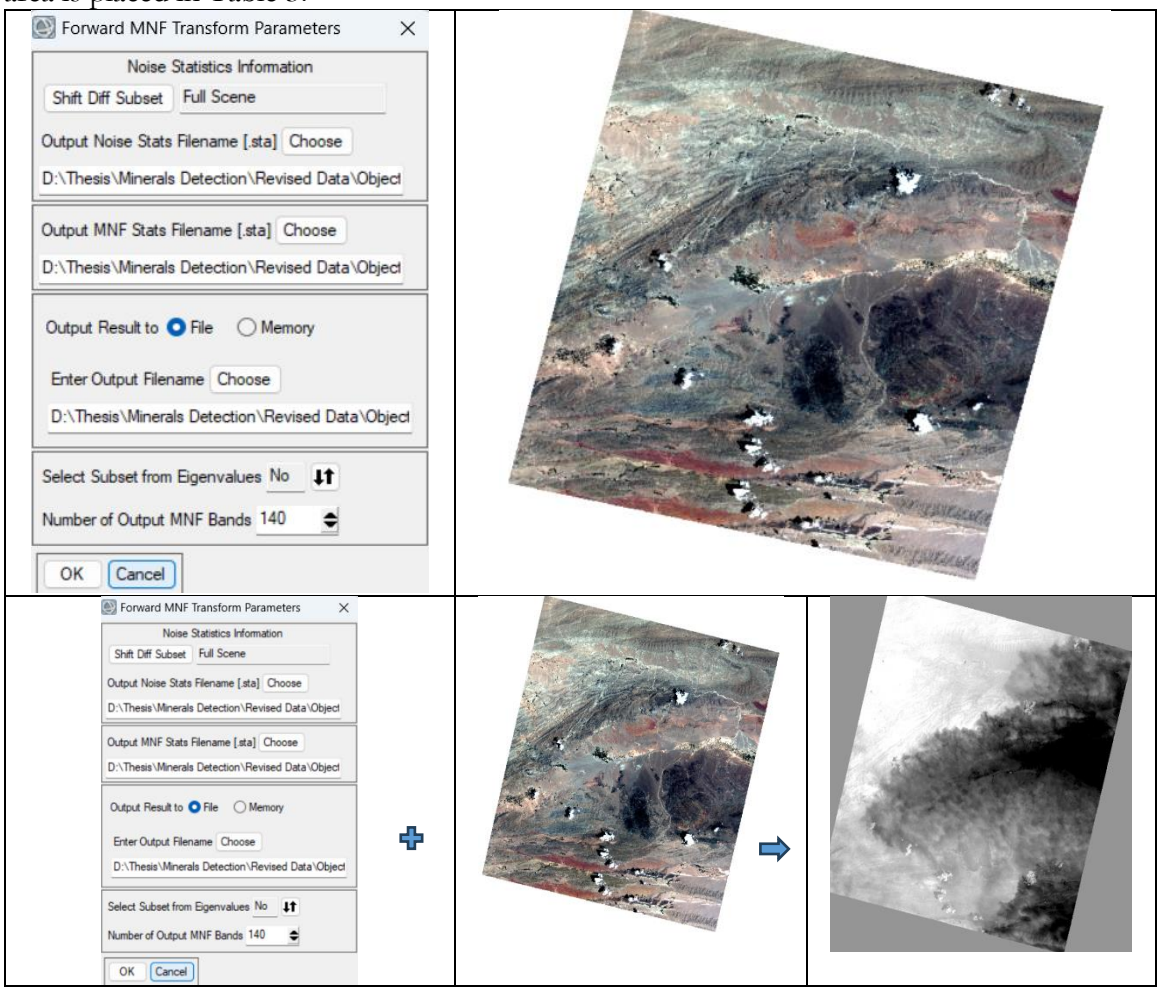

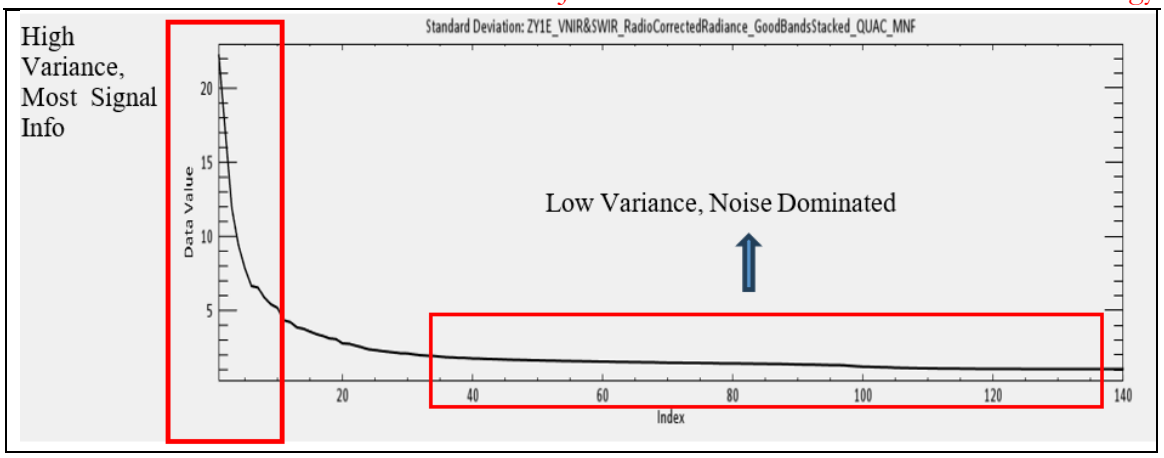

(a)

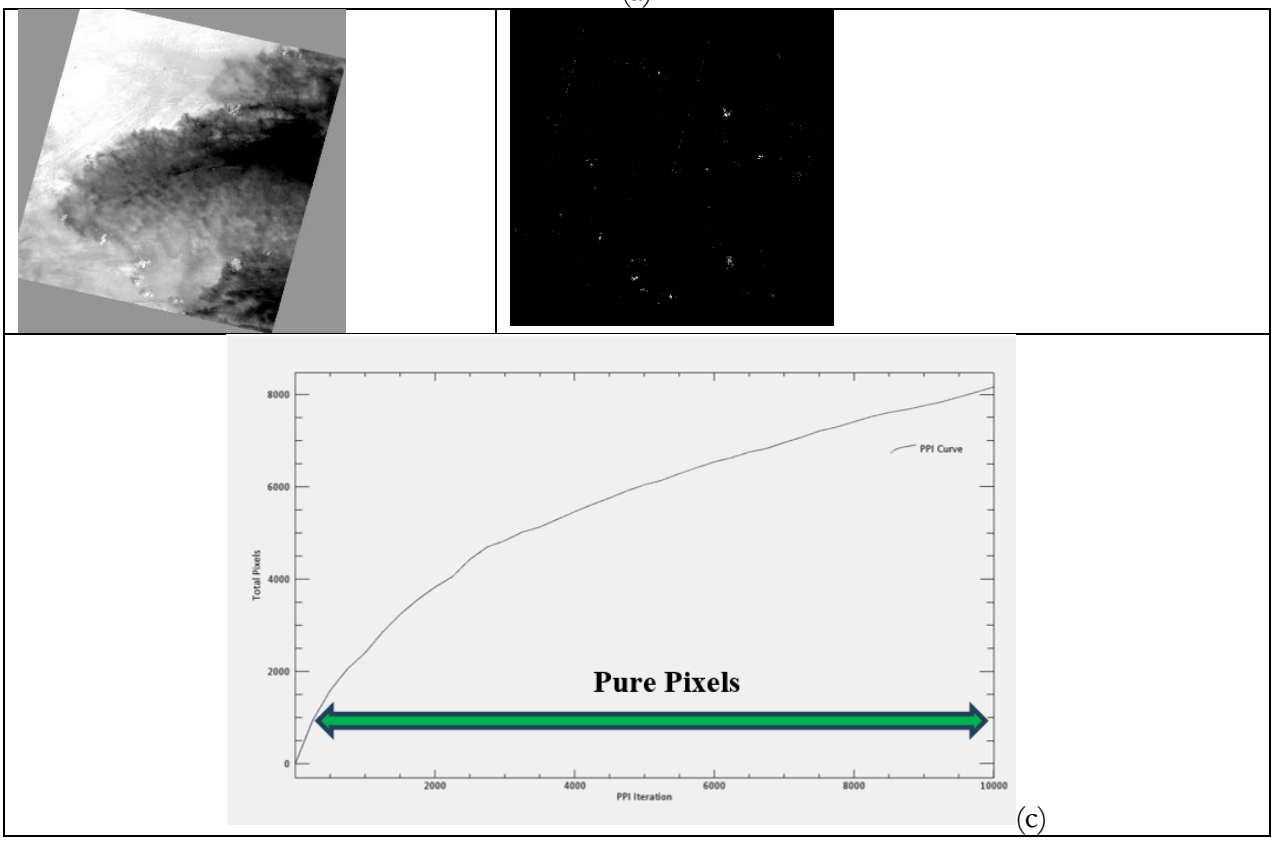

(c)

Figure 5. End member extraction steps (a) MNF Transformation and variance curve showing most informative bands, (b) MNF transformed image is processed for PPI, and 1000 iterations are run to get pure pixels.

Table 2. Diagnostic absorption features of desired materials.

Material/ Material	Wavelengths (nm)	Diagnostic Absorption Features
Serpentine	1400 nm (weak), 2300–2320 nm (strong/doublet)	Strong doublet in the 2.3 μm region
Chromite	400–500 nm, 1000–1200 nm	Broad dip toward shorter λ beyond 1100 nm
Magnesite	1890 nm (weak), 2320–2350 nm, 2520 nm (strong)	Sharp 2.3–2.5 μm carbonate absorptions

Magnetite	Very low reflectance, dip at 850–1000 nm	Flat dark spectrum across VNIR
Quartz	High, flat reflectance in VNIR–SWIR; strong features in TIR (8–10 μm)	Featureless in VNIR–SWIR; used as spectral reference
Kaolinite	1400 nm, 2165–2175 nm, 2200–2210 nm (doublet)	Sharp doublet near 2.2 μm
Montmorillonite	1900 nm (broad), 2200–2210 nm	Broader 2.2 μm feature than kaolinite
Calcite	1950 nm (weak), 2330–2340 nm, 2550 nm (strong)	2.34 μm carbonate dip; deeper than dolomite
Dolomite	1880 nm, 2320–2325 nm, 2520 nm	2.32 μm dip (slightly blue-shifted vs calcite)
Vegetation	450, 670 nm (absorb); 550 nm (reflect); rise at 680–750 nm dips at 1400, 1900, 2100–2300 nm	Red-edge + high NIR + SWIR water absorption

Spectral Matching:

Spectral matching is the process of comparing an unknown spectrum (from a pixel in the image or a lab sample) to a known library of reference spectra, e.g., from the USGS spectral library, to determine its identity [38]. Spectral matching critically relies on the presence and characteristics of diagnostic absorption features. Accordingly, based on Geological settings together with known lithologies of the study area (as acquired from the Geological Survey of Pakistan), exploration of minerals including chromite, serpentine, magnetite, magnesite, quartz, kaolinite, montmorillonite, calcite, and dolomite was envisaged. First of all, spectral profiles of individual minerals duly matching the USGS library were collected, and finally, the cumulative spectra were prepared. Separate spectral libraries for the USGS library and individual spectra of expected minerals in our study area, using ZY1E satellite imagery and multispectral datasets, were prepared.

Minerals Identification and Lithologies Zoning:

Based on peculiar diagnostic absorption features and spectral matching [94], spectral libraries of pixels extracted from hyperspectral and multispectral imageries are prepared [95][96]. These libraries served as training datasets for subsequent classification and mapping of minerals and lithologies. Traditionally, geologists used to identify lithologies through field observations and physical samples, followed by geochemical analysis [97]. Nevertheless, owing to acute difficulties in accessing hilly, rugged terrain areas, limited resources, and security threats, physical visits are very difficult [98]. Therefore, using a verified means of Remote Sensing, the principle of alteration minerals is used for minerals & lithologies identification. In geology, alteration is the mineralogical as well as chemical alteration of a rock amid its interaction/ reaction with hydrothermal fluids, heat, or gases, which leads to the formation of distinct alteration minerals & lithologies serving as fingerprints or pathfinders to discover underlying original/ actual deposits. The most common alteration types, their key minerals, and lithological settings are summarized in Table 4. A geological map showing the lithologies of Baluchistan province was acquired from GSP in JPEG format and then digitized (shapefile) in ArcMap. Thereafter, a lithological map was created having different polygons showing different lithologies of the study area (Figure 6) in line with GSP provided geological map of Pakistan. Most of the areas contain ophiolites, limestone, sandstone, and shale types of lithology.

Table 4. Alteration minerals types and common settings.

Alteration Type	Key Minerals	Common Setting

Potassic (K-silicate)	K-feldspar, Biotite, Magnetite, Quartz	Porphyry Cu-Au core
Phyllic (Sericitic)	Sericite, Quartz, Pyrite, Chlorite	Porphyry halo
Propylitic	Chlorite, Epidote, Calcite, Albite, Hematite	Distal ore halo
Argillic	Kaolinite, Montmorillonite, Illite	Shallow epithermal
Advanced Argillic	Alunite, Pyrophyllite, Dickite, Quartz	High-sulfidation epithermal
Silicification	Microcrystalline Quartz, Chalcedony, Opal	Veins/Stockworks
Carbonatization	Calcite, Dolomite, Ankerite, Siderite	Shear zones/Greenstones
Greisenization	Quartz, Muscovite, Topaz, Fluorite	Sn, W, Mo deposits
Skarn Formation	Garnet, Pyroxene, Epidote, Wollastonite	Intrusion-carbonate contact
Chloritization	Chlorite, Epidote, Actinolite	Propylitic zones
Serpentinization	Chrysotile, Lizardite, Antigorite	Ultramafic rocks
Hematitization	Hematite, Goethite	Oxidized zones

Results:

Efficacy of hyperspectral (ZY1E) vis-à-vis multispectral (ASTER, Sentinel-2, Landsat-8) datasets for alteration minerals detection as well as lithological mapping was evaluated in the Qilla Saifullah district with a deep focus on the Muslim Bagh ophiolite complex. Spectral signatures were collected for each imagery (training samples) and different classification/ minerals identification techniques, i.e., Spectral Angle Mapper (SAM), Spectral Feature Fitting (SFF), Support Vector Machine (SVM), Random Forest (RF), and Band Ratios were used, particularly for ZY1E/ hyperspectral dataset. However, for multispectral datasets, SAM, SFF, and Band Ratios were used for the identification/ extraction of minerals. Continuous spectral coverage of ZY1E hyperspectral imagery, i.e., 400nm to 2500nm (Table 5), proved convenient for near actual/ perfect extraction of spectral profiles of expected minerals. A comparative chart (Figure 7) showing spectral coverage of all datasets used reveals the absence of a vast SWIR region in multispectral imagery.

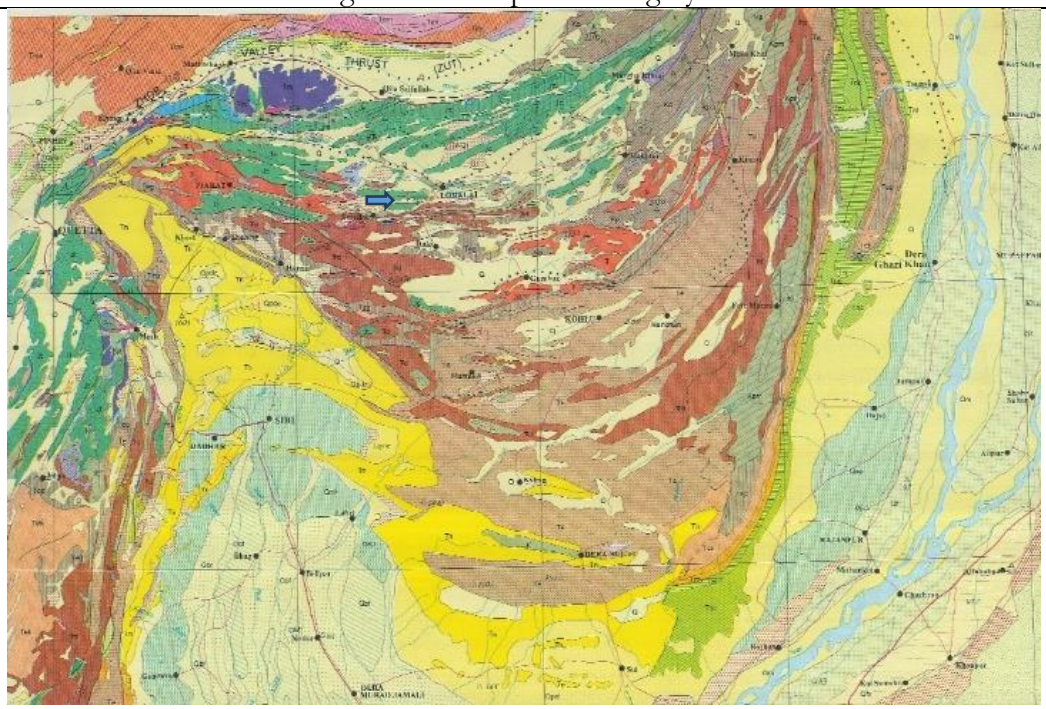

(a)

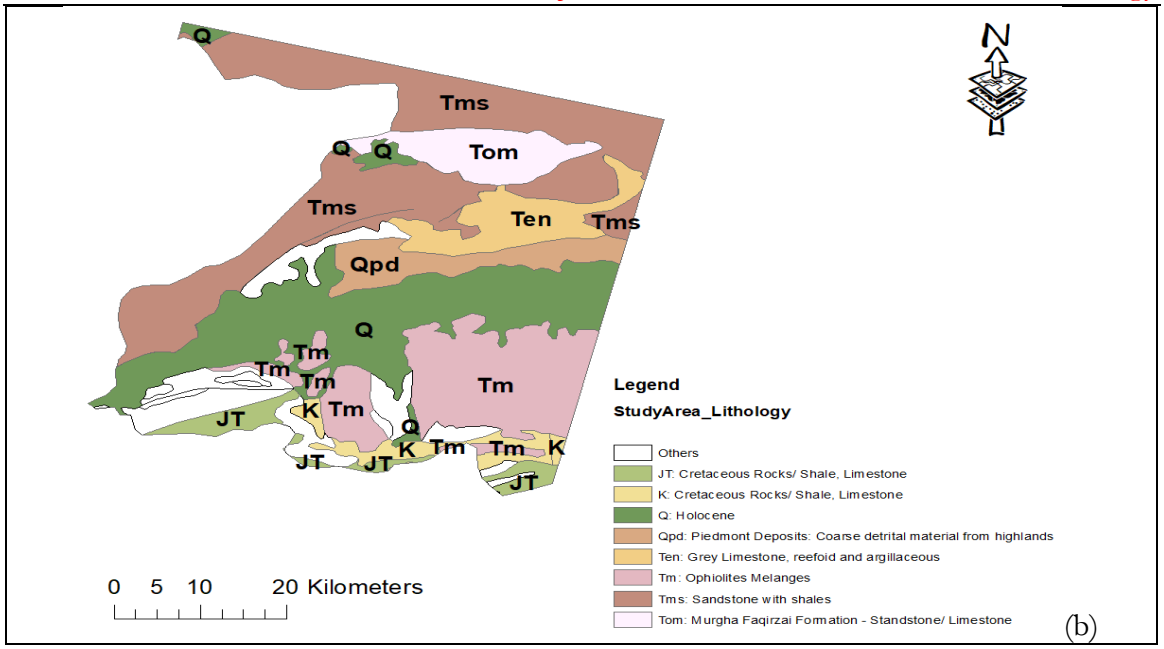

Figure 6. a. Geological Survey of Pakistan provided a geological map, b. Digitized study area map with lithologies.

Table 3. ZY1E satellite specifications.

Satellite Payloads	ZY1E
Launch date	2019-09-12
Orbit altitude (km)	778
Number of bands	76 (VNIR), 90 (SWIR)
Spectral range (µm)	0.4-1.0 (VNIR), 1.0-2.5 (SWIR)
Spectral resolution (nm)	10 (VNIR), 20 (SWIR)
Spatial resolution (m)	30
Revisit period (days)	55
Swath width (km)	60
Signal-to-noise ratio (SNR)	≥240 (0.4-0.9 µm) ≥180 (0.9-1.75 µm) ≥120 (1.75-2.50 µm)

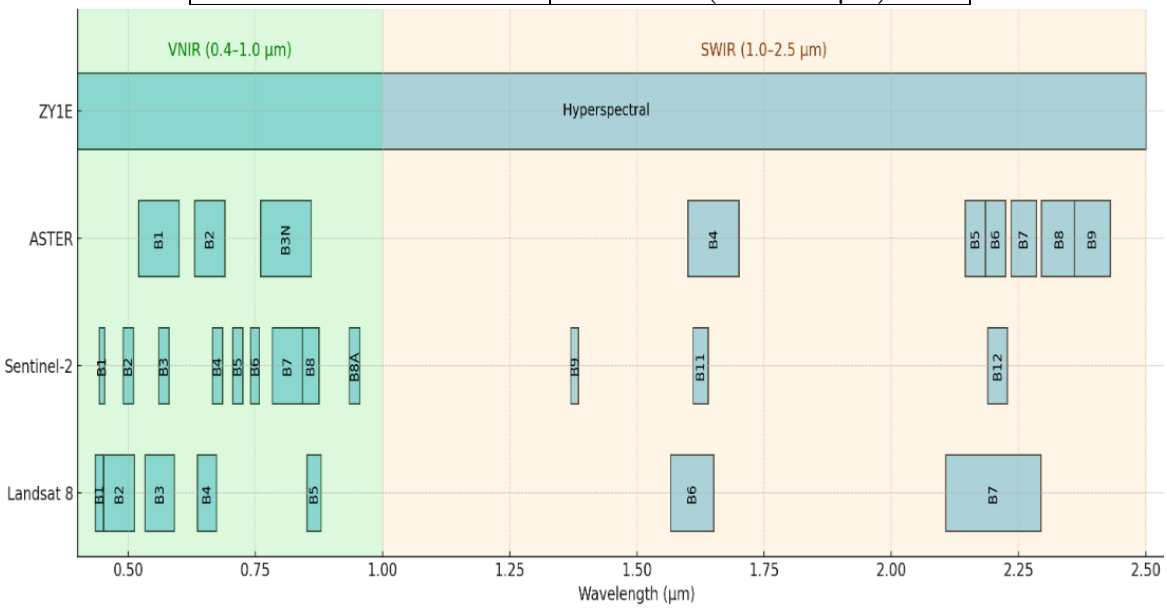

Figure 7. Comparative chart showing spectral coverage of all datasets being used in research.

A spectral library of expected minerals in our study area was generated using diagnostic absorption features and spectral matching principles, followed by classification using SAM, SVM, and RF. Spectral profiles of USGS and ZY1E imageries are shown in Figure 8. Ground truthing data (point data) acquired from the field survey by GSP was overlaid on the classified images to visualize how many mineral points (field survey data) exactly fall on classified minerals. SAM showed strong performance due spectral based classification. Nevertheless, SVM and RF also yielded higher accuracy against tuned parameters. For minerals classification, 81.82% accuracy was achieved, 86.11% accuracy was observed towards lithologies classification. Here, SAM turned out to be the best classifier with 81.82% accuracy. A comparative table showing different classifiers' accuracy and kappa coefficients is shown in Table 6. It is to be noted that the spatial resolution of ZY1E imagery is 30m, and each pixel and its spectral profile were generated of 30m ground distance. Each pixel represents a 30m x 30m area. Whereas ground sampling was done on small points (2-3m distance). Hence, it is deduced that low spatial resolution is one of the reasons for low accuracy for mineral classification. By increasing the spatial resolution, accuracy could be improved effectively. Minerals and lithology maps were also generated (Figure 9) from ZY1E imagery. Additionally, SFF and band ratios were also used to ascertain the minerals' presence through different techniques. It focuses on the depth and shape of absorption features in mineral-diagnostic wavelengths, rather than the entire spectral curve. Higher Scale value & Low RMS values are desired for accurate identification of minerals. Results of SFF and band ratios also validate the presence of desired minerals in our study area. Montmorillonite, Kaolinite, Chromite, and Magnesite showed higher scale values. SFF classification results for ZY1E are shown in Table 7. Band ratio showed excellent results for the identification of magnesite, magnetite, serpentine, and chromite. A detailed summary of band ratios/ indices along with wavelengths for hyperspectral and multispectral datasets is shown in Table 8. Only hyperspectral covers the desired minerals' diagnostic absorption wavelength range. Comparative assessment of band ratios results is also shown in Figure 12.

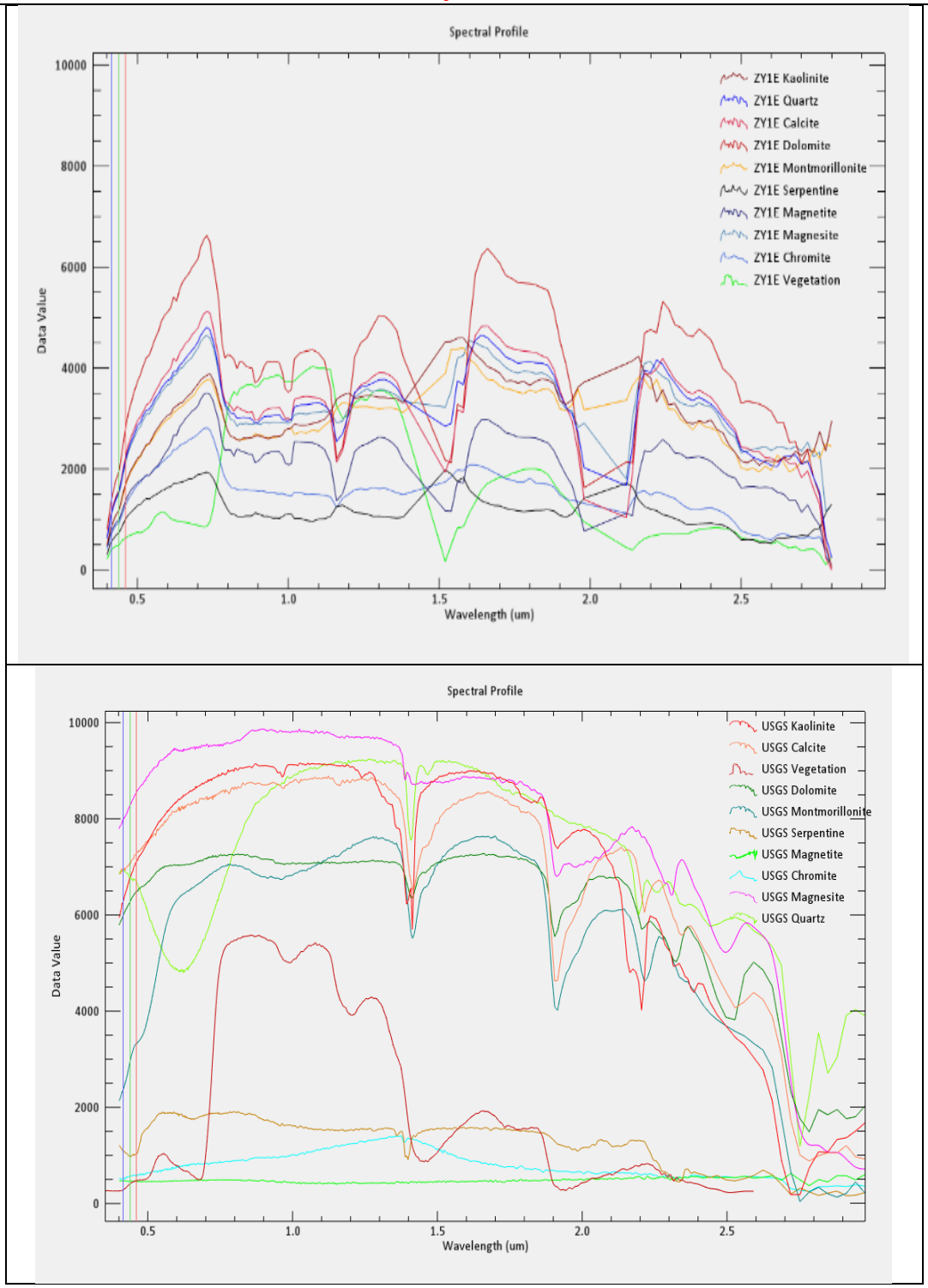

Figure 8. Spectral Libraries a. Spectral profiles of expected minerals, b. USGS Spectral library of expected minerals.

Table 6. Comparative summary of different classifiers' accuracy.

Classifier	Accuracy	Kappa Factor
Original SAM	73.91 %	0.636
Initial RF	72.73 %	0.633
Tuned RF	63.64 %	0.532
Tuned SVM	81.82 %	0.761

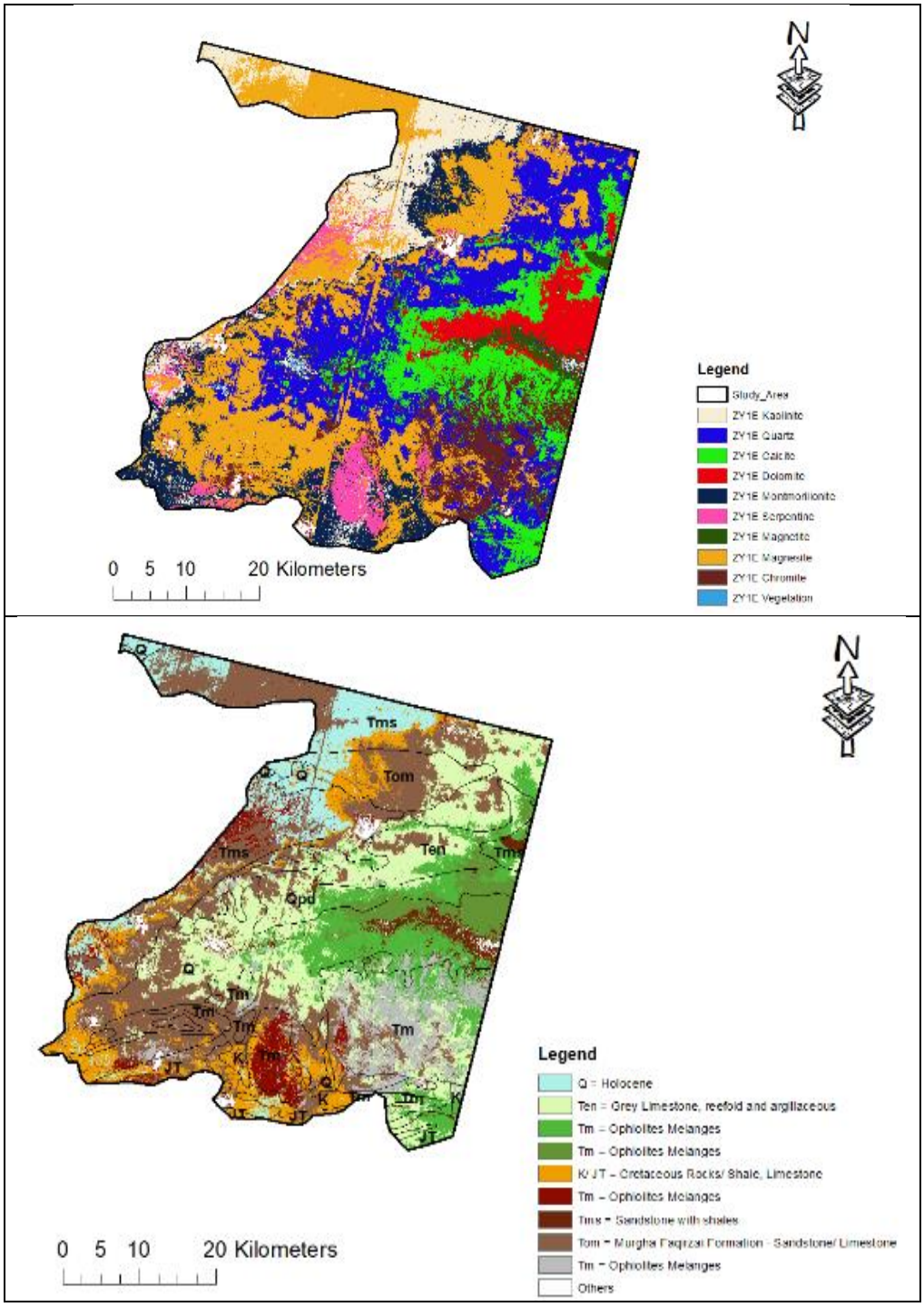

Figure 9. Maps generated using spectral angle mapper classifier, a. ZY1E minerals map, b. ZY1E lithology map.

Table 4. SFF classification (ZY1E) showing scale and RMS values, generated using spectral signatures.

Mineral	Scale				RMS			
	MIN	MAX	MEAN	SD	MIN	MAX	MEAN	SD
Quartz	0.15	3.00	1.01	0.17	0.01	0.61	0.09	0.06
Serpentine	0.10	2.23	0.60	0.17	0.00	0.45	0.12	0.05
Magnetite	0.12	2.63	0.87	0.16	0.00	0.65	0.12	0.07

Magnesite	0.16	3.24	1.06	0.19	0.00	0.57	0.09	0.05
Chromite	0.13	2.86	0.94	0.17	0.00	0.58	0.09	0.05
Vegetation	0.10	1.79	0.28	0.10	0.00	0.61	0.23	0.04
Kaolinite	0.15	3.49	1.00	0.25	0.00	0.48	0.11	0.04
Calcite	0.12	2.50	0.85	0.15	0.00	0.65	0.11	0.0 5
Dolomite	0.10	2.32	0.79	0.14	0.00	0.65	0.11	0.07
Montmorillonite	0.17	3.76	1.11	0.26	0.02	0.49	0.10	0.04

Among multispectral imageries, except for ASTER, the remaining multispectral sensors (Sentinel-2 and Landsat-8) could not identify the expected minerals with higher accuracy in our study area due to limited SWIR coverage. ASTER proved to be the most effective dataset due to its six SWIR bands, enabling superior detection of OH-, Al-, and carbonate-bearing minerals. Serpentine, magnetite, carbonates (calcite, dolomite, magnesite), and uniquely enabling quartz identification due to its TIR coverage proved helpful in ASTER Imagery. Landsat-8 delivered balanced yet moderate performance, detecting carbonates (calcite, dolomite, magnesite) and Mg–OH minerals (serpentine) reasonably well but was limited by its broader bands and shorter SWIR cutoff at 2.30 µm. Sentinel-2 performed best as a complementary dataset, offering acceptable detection for clays (kaolinite, montmorillonite) and some carbonates (calcite, dolomite), but underperforming for minerals with absorption features beyond 2.19µm. Mineral maps using spectral profiles from these multispectral sensors/ images were also generated (Figures 10 to 12). Spectral Feature Fitting (SFF) and band ratios further confirmed ASTER's relative advantage. SFF results (Scale and RMS values) are shown in Tables 8 to 9. Higher scale value and low RMS value indicate better detection of minerals. Overall, magnesite, chromite, and magnetite were identified accurately. Band ratios/ indices (already shown in Table 8) are shown in Figure 13. These results validate the absence of precise identification of spectral profiles in multispectral datasets due to limited bands/ spectral coverage. Band ratios proved helpful for chromite and serpentine identification. Alteration minerals were used as proxies to delineate the lithologies of the study area. Overall comparison of all sensors with respect to performance/ detection of minerals (rated out of 10) is also explained in Figure 14.

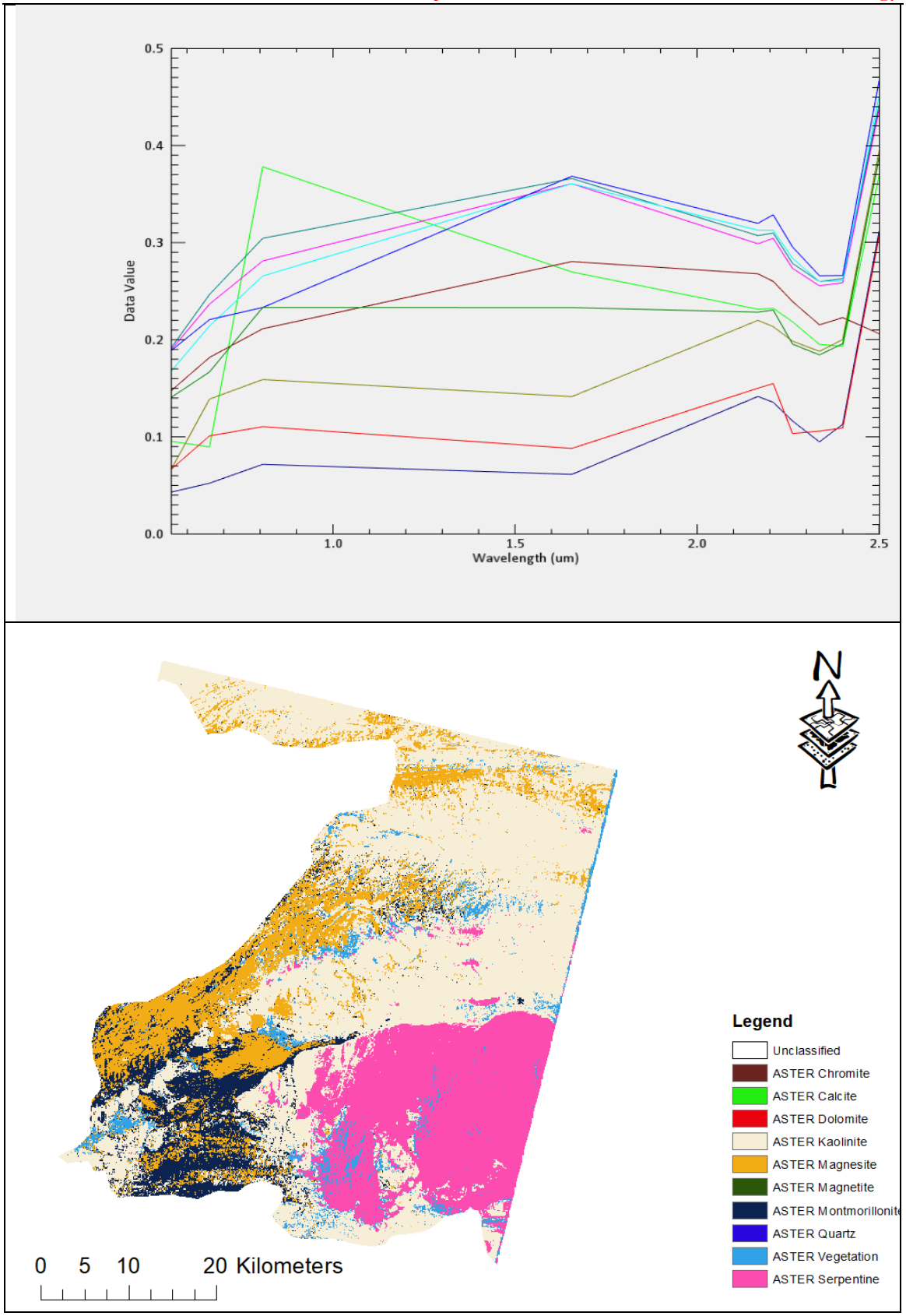

Figure 10. Spectral signatures collected from ASTER imagery, Minerals map generated using spectral angle mapper classifier (ASTER)

Table 5. Band ratios/ indices of all datasets being used in research.

Minerals	ZY1E		ASTER		Sentinel-2		Landsat-8	
	Band Ratios	Wavelengths	Band Ratios	Wavelengths	Band Ratios	Wavelengths	Band Ratios	Wavelengths
Chromite	b21/b6	600/450	b2/b1	660/560	b4/b3	-	b4/b2	562/443
Magnetite	(b5-b10)/ (b5+b10)	(1100 -1200)/ (1100 + 1200)	b5/b4	-	(b4/b2)	-	(b10-b11)/ (b10+b11)	10.89-12.00/ 10.89-12.00
Magnesite	(b67-b72)/ (b67+b72)	(2340 -2440)/ (2340 + 2440)	(b8-b9)/ (b8+b9)	(2330-2395/ (2330+2395)	(b11/b12)	-	b6/b7	-
Serpentine	(b60-b49)/ (b60+b49)	(2200-2000)/ (2200+2000)	(b6+b9)/ (b7+b8)	-	(b11/b12)	-	(b6+b7)/b5	-
Quartz	(b55-b60)/ (b55+b60)	(2100 -2200)/ (2100 + 2200)	(b11/ (b10+b12))	-	b12-b11/ b12+b11	2190-1610/ 2190+1610	-	-
Kaolinite	(b144-136)/ (b144+b136)	(2200-2100)/ (2200+2100)	b4/b6	-	b11/b12	-	-	-
Montmorillonite	(b144-151)/ (b144+b151)	(2200- 2300)/ (2200+2300)	b7/b6	-	b11/b12	-	-	-
Calcite	(b154-163)/ (b154+b163)	(2340 -2450)/ (2340+2450)	(b6+b8)/b7	-	(b11/b12	-	b6/b7	-
Dolomite	(b154-163)/ (b154+b163)	(2340-2450)/ (2340 + 2450)	b8/b7	-	-	-	-	-

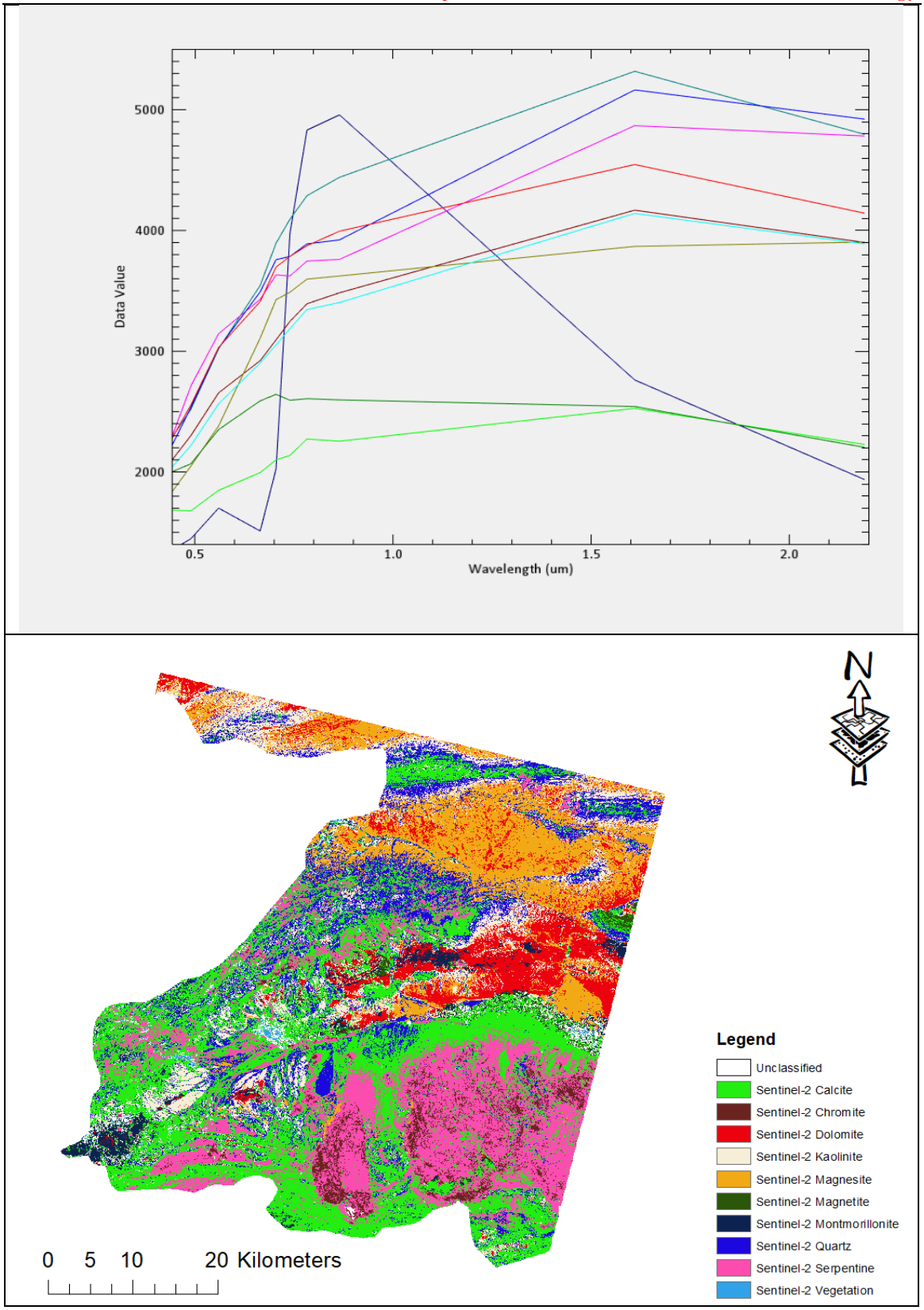

Figure 11. a. Spectral signatures collected from Sentinel-2 imagery, b. Minerals map generated using spectral angle mapper classifier (Sentinel-2)

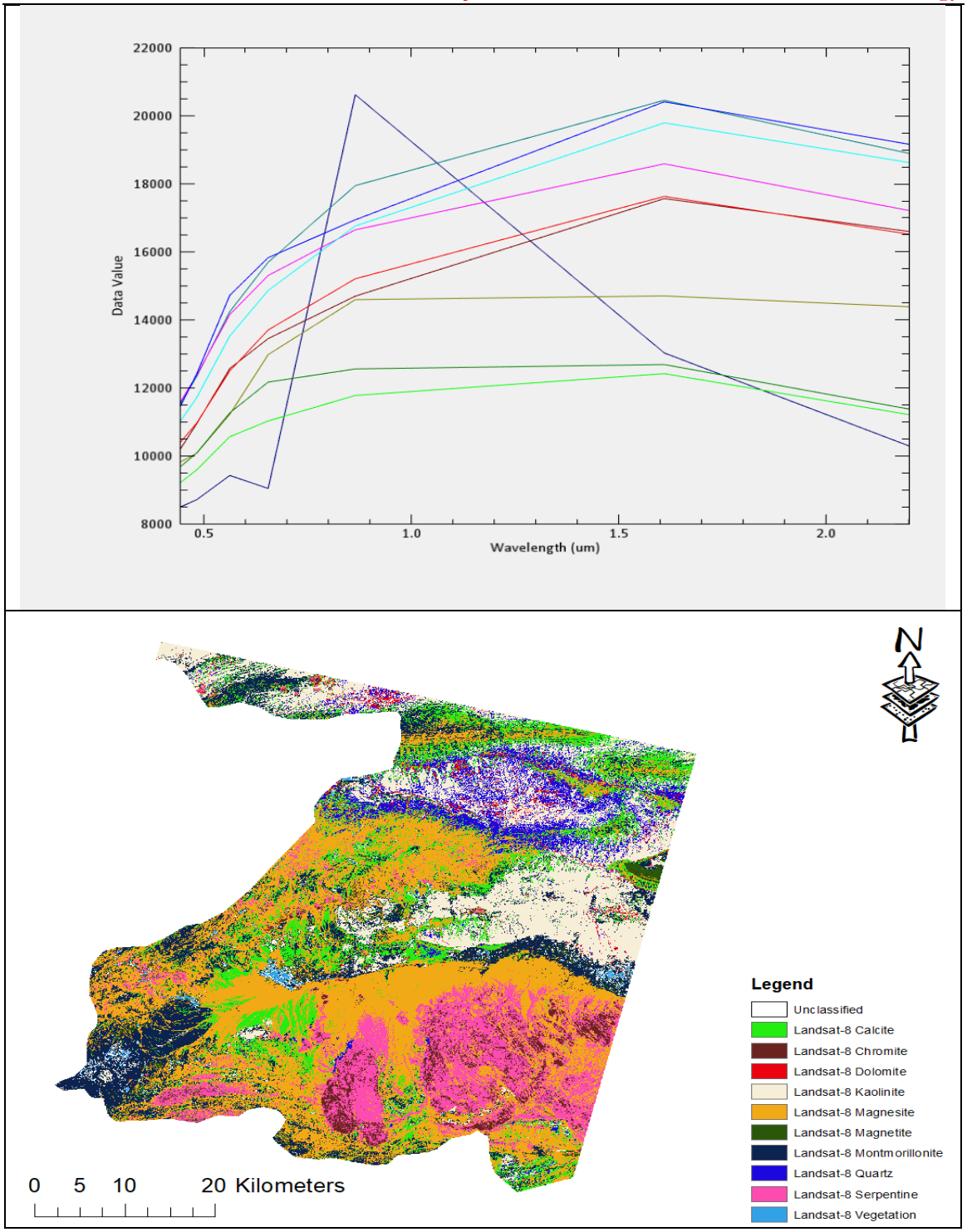

Figure 12. a. Spectral signatures collected from Landsat-8 imagery, b. Minerals map generated using spectral angle mapper classifier (Landsat-8)

Table 9. Spectral Feature Fitting classification (ASTER) showing scale and RMS values.

Mineral	Scale				RMS			
	MIN	MAX	MEAN	SD	MIN	MAX	MEAN	SD
Quartz	0.15	3.00	1.01	0.17	0.01	0.61	0.09	0.06
Serpentine	0.10	2.23	0.60	0.17	0.00	0.45	0.12	0.05
Magnetite	0.12	2.63	0.87	0.16	0.00	0.65	0.12	0.07
Magnesite	0.16	3.24	1.06	0.19	0.00	0.57	0.09	0.05

Chromite	0.13	2.86	0.94	0.17	0.00	0.58	0.09	0.05
Vegetation	0.10	1.79	0.28	0.10	0.00	0.61	0.23	0.04
Kaolinite	0.15	3.49	1.00	0.25	0.00	0.48	0.11	0.04
Calcite	0.12	2.50	0.85	0.15	0.00	0.64	0.12	0.07
Dolomite	0.10	2.32	0.79	0.14	0.00	0.65	0.11	0.07
Montmorillonite	0.17	3.76	1.11	0.26	0.02	0.49	0.10	0.04

Table 10. Spectral Feature Fitting classification (Sentinel-2) showing scale and RMS values.

Mineral	**Scale**				**RMS**			
	MIN	**MAX**	**MEAN**	**SD**	**MIN**	**MAX**	**MEAN**	**SD**
Quartz	0.00	28.73	0.85	1.96	0.00	0.28	0.01	0.01
Serpentine	0.00	14.51	0.36	0.70	0.00	0.23	0.01	0.01
Magnetite	0.00	11.63	0.19	0.57	0.00	0.28	0.01	0.02
Magnesite	0.00	19.13	0.71	0.75	0.00	0.33	0.01	0.02
Chromite	0.00	18.77	0.36	0.53	0.00	0.31	0.01	0.02
Vegetation	0.00	1.19	0.03	0.08	0.00	0.24	0.01	0.01
Kaolinite	0.00	46.73	1.33	2.46	0.00	0.25	0.01	0.01
Calcite	0.00	23.40	0.81	1.63	0.00	0.32	0.01	0.01
Dolomite	0.00	21.54	0.90	0.99	0.00	0.32	0.01	0.02
Montmorillonite	0.00	19.48	0.62	1.25	0.00	0.30	0.01	0.02

Table 11. Spectral Feature Fitting classification (Landsat-8) showing scale and RMS values.

Mineral	**Scale**				**RMS**			
	MIN	**MAX**	**MEAN**	**SD**	**MIN**	**MAX**	**MEAN**	**SD**
Quartz	0.15	3.00	1.01	0.17	0.01	0.61	0.09	0.06
Serpentine	0.10	2.23	0.60	0.17	0.00	0.45	0.12	0.05
Magnetite	0.12	2.63	0.87	0.16	0.00	0.65	0.12	0.07
Magnesite	0.16	3.24	1.06	0.19	0.00	0.57	0.09	0.05
Chromite	0.13	2.86	0.94	0.17	0.00	0.58	0.09	0.05
Vegetation	0.10	1.79	0.28	0.10	0.00	0.61	0.23	0.04
Kaolinite	0.13	1.87	0.94	0.17	0.00	0.68	0.09	0.05
Calcite	0.10	1.32	0.60	0.17	0.00	0.65	0.12	0.05
Dolomite	0.12	1.53	0.87	0.16	0.00	0.85	0.12	0.07
Montmorillonite	0.11	1.66	0.28	0.10	0.00	0.64	0.23	0.04

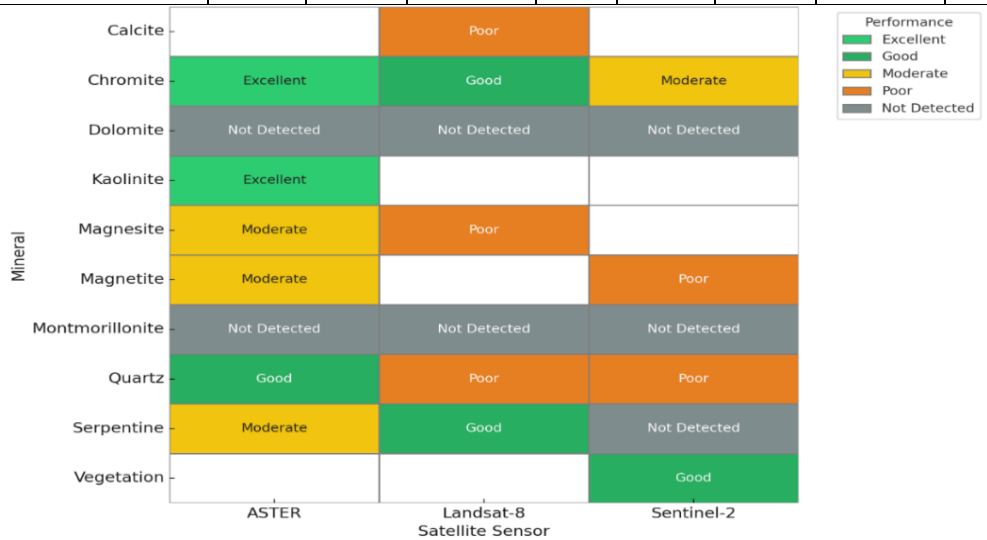

Figure 13. Band ratios/ indices performance w.r.t minerals detection in multispectral sensors.

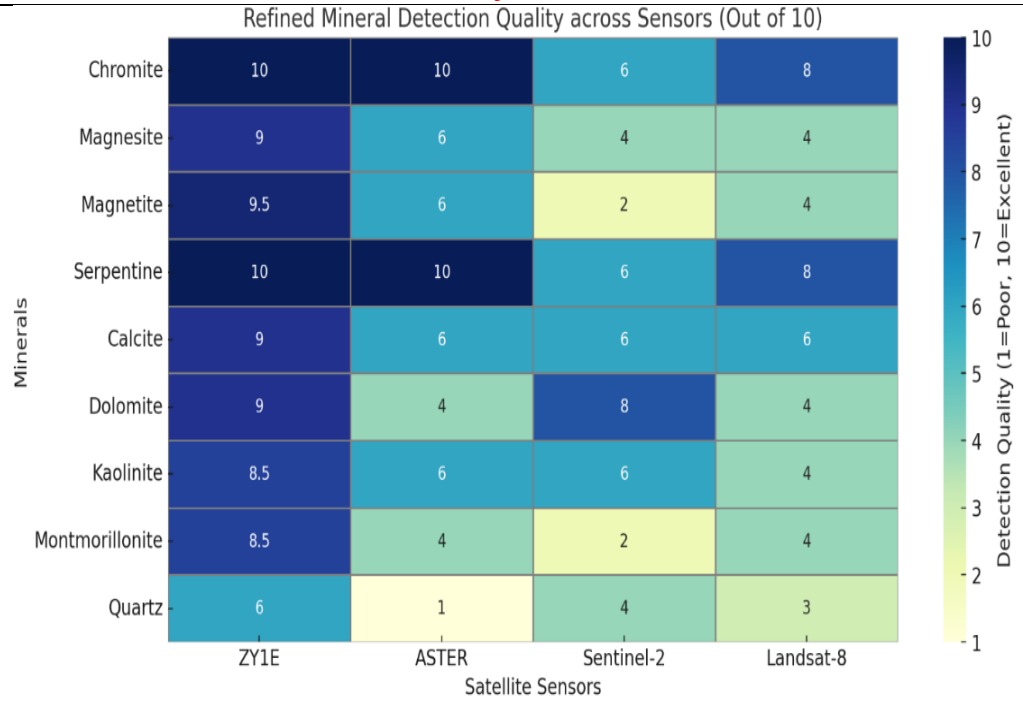

Figure 14. Overall minerals detection performance of all sensors.

Discussion:

Although ASTER provided a cost-effective alternative for alteration minerals mapping, yet hyperspectral imagery outperformed multispectral sensors (ASTER, Sentinel-2 & Landsat-8) in mineral discrimination due to continuous, high-spectral-resolution coverage (0.4µm – 2.5µm) across the VNIR and SWIR regions using Diagnostic Absorption Features of ophiolitic minerals. Ophiolites show narrow, mineral-specific absorption features/ bands, which cannot be distinguished through multispectral sensors due to limited spectral coverage. Whereas, hundreds of contiguous narrow bands of hyperspectral sensor (ZY1E) enable us to precisely extract absorption band position, depth, width, and asymmetry through diagnostic absorption feature analysis. Thereby, allowing for direct spectral matching with laboratory-measured reference spectra from the USGS spectral library. Therefore, reducing spectral mixing and misclassification. Additionally, ZY1E imagery combined with physics-based spectral classifiers such as Spectral Angle Mapper (SAM) and Spectral Feature Fitting (SFF) gives more precise results because these classifiers rely on full spectral shape rather than band-integrated reflectance values. These classifiers are inherently constrained when applied to multispectral datasets due to insufficient spectral dimensionality. It also implies that although machine-learning approaches (e.g., Random Forest) give improved outcomes for multispectral classification, their performance remains limited due to the absence of key diagnostic SWIR bands. Thus, it further shows that complex algorithms cannot compensate for inadequate spectral resolution. The band ratio approach proved a rapid and effective tool for preliminary detection, but lacked hyperspectral precision. Key findings of this research can be summarized as (1) Hyperspectral (ZY1E) imagery is indispensable for high-accuracy mineral and lithological mapping in ophiolitic terrains. (2) ASTER provides the most reliable multispectral alternative when hyperspectral data is unavailable. (3) Integration of SAM, SVM, RF, and SFF enhances classification robustness. (4) Diagnostic absorption features and spectral libraries remain critical for validating remote sensing mineral maps. Hence, it is established that hyperspectral datasets serve as a benchmark for mineral exploration in inaccessible regions, with multispectral data serving as complementary resources.

Recommendations:

Future studies should incorporate ground-based spectral calibration using handheld spectroradiometers and laboratory-analyzed rock samples to develop context-specific reference spectra that better represent mineral aggregates and improve classification reliability. Establishing a local spectral library at the institutional level (e.g., NUST) or through industry collaboration is strongly recommended to support long-term mineralogical research and advanced 3D mapping initiatives in Pakistan. Emerging hyperspectral missions such as EnMAP and EMIT, with improved spectral fidelity, should be prioritized for detailed mineral discrimination, while ASTER can serve as a cost-effective first-line dataset for preliminary exploration and target prioritization. Finally, broader access to licensed geospatial software (e.g., ENVI) and its integration with GIS platforms such as ArcGIS would enable the development of customized analytical workflows, enhancing operational efficiency and exploration decision-making.

Conclusion:

Comparative efficacy of hyperspectral (ZY1E) and multispectral (ASTER, Landsat-8, Sentinel-2) datasets is demonstrated in this study for mineral detection and lithological inference. Comprehensive preprocessing, i.e., geometric, radiometric, and atmospheric corrections, followed by dimensionality reduction (MNFT, PPI, nD Visualization) ensured reliable data quality. Among classification techniques, both Spectral Angle Mapper (SAM) and Support Vector Machine (SVM) yielded promising results, with SVM achieving the highest overall accuracy (81.82%) against mineral point data. Lithological classification, inferred through hydrothermal alteration minerals, attained an accuracy of 86.11%. Secondary methods, including Spectral Feature Fitting (SFF) and band ratios, further strengthened these results, particularly for clays, carbonates, and Mg–OH minerals.

Sensor-wise, ZY1E proved superior due to its contiguous narrow spectral bands (0.4–2.5 μm), enabling precise species-level mineral identification. Among multispectral sensors, ASTER emerged as the strongest alternative candidate offering consistent detection of carbonates, Mg–OH minerals, and a unique capability for quartz through its TIR coverage. Owing to limited spectral coverage, Landsat-8 and Sentinel-2 demonstrated complementary participation against minerals determination; however, these sensors could be helpful against spatial and temporal coverages for other applications. Collectively, these findings reiterate that strategic integration of hyperspectral and multispectral datasets provides a cost-effective and reliable framework for mineral exploration, particularly in geologically complex terrains. It is worth mentioning that these findings also align with previous researches, hence, emphasizing the diagnostic power of hyperspectral sensors (Kruse et al., 1993; Clark et al., 2003) [99], the utility of ASTER [100] in alteration mineral mapping (Rowan & Mars, 2003; Pour & Hashim, 2015), and the continued importance of Landsat and Sentinel-2 for broad-scale geological applications (Van der Meer et al., 2012; Kirsch et al., 2018) [101][102].

Disclosures:

The authors declare that they have no known competing financial interests or personal relation- ships that could have appeared to influence the work reported in this paper.

Code, Data, and Materials Availability:

The raw data supporting the conclusions of this paper can be obtained from the corresponding author.

Acknowledgments:

We are thankful for support from the Geological Survey of Pakistan (GSP) for the provisioning of field data & geological maps, and step-by-step guidance from supervisors and university staff for technical resources and institutional support. Their cooperation significantly facilitated the research process and enhanced the credibility of the findings.

References:

[1] M. S. Malkani, "Revised Stratigraphy and Mineral Resources of Balochistan Basin, Pakistan: An Update," *Open J. Geol.*, vol. 10, no. 7, pp. 784–828, 2020, [Online]. Available: https://www.researchgate.net/publication/343284097_Revised_Stratigraphy_and_Mineral_Resources_of_Balochistan_Basin_Pakistan_An_Update

[2] "Heron, A.M. (1950) Directory of Economic Minerals. Geological Survey of Pakistan, Record, 1, Part II, 1-69. - References - Scientific Research Publishing." Accessed: Jan. 11, 2026. [Online]. Available: https://www.scirp.org/reference/referencespapers?referenceid=3921348

[3] "Ahmad, Z. (1969) Directory of Mineral Deposits of Pakistan. Geological Survey of Pakistan, Record, 15, 1-200. - References - Scientific Research Publishing." Accessed: Jan. 11, 2026. [Online]. Available: https://www.scirp.org/reference/referencespapers?referenceid=2766118

[4] "Gauher, S.H. (1969) Economic Minerals of Pakistan A Brief Review. Geological Survey of Pakistan, Pre Publication Issue 88, 1-110. - References - Scientific Research Publishing." Accessed: Jan. 11, 2026. [Online]. Available: https://www.scirp.org/reference/referencespapers?referenceid=2805555

[5] M. Abrams and Y. Yamaguchi, "Twenty years of ASTER contributions to lithologic mapping and mineral exploration," *Remote Sens.*, vol. 11, no. 11, Jun. 2019, doi: 10.3390/RS11111394.

[6] "Metallogeny and Mineral Potential of Pakistan." Accessed: Jan. 11, 2026. [Online]. Available:https://www.researchgate.net/publication/393744495_Metallogeny_and_Mineral_Potential_of_Pakistan

[7] "Mineral Resources of Pakistan: A Review." Accessed: Jan. 11, 2026. [Online]. Available: https://www.researchgate.net/publication/305942087_Mineral_Resources_of_Pakistan_A_Review

[8] "Mineral Resources of Pakistan: Provinces and Basins wise." Accessed: Jan. 11, 2026. [Online].Available:https://www.researchgate.net/publication/315834509_Mineral_Resources_of_Pakistan_Provinces_and_Basins_wise

[9] "Mineral Resources of Pakistan-an update." Accessed: Jan. 11, 2026. [Online]. Available: https://www.researchgate.net/publication/315707448_Mineral_Resources_of_Pakistan-an_update

[10] "Stratigraphy, Mineral Potential, Geological History and Paleobiogeography of Balochistan Province, Pakistan." Accessed: Jan. 11, 2026. [Online]. Available: https://www.researchgate.net/publication/282330367_Stratigraphy_Mineral_Potential_Geological_History_and_Paleobiogeography_of_Balochistan_Province_Pakistan

[11] "Mineral Resources of Balochistan Province, Pakistan." Accessed: Jan. 11, 2026. [Online]. Available:https://www.researchgate.net/publication/315834485_Mineral_Resources_of_Balochistan_Province_Pakistan

[12] "Reconnaissance geology of part of west Pakistan." Accessed: Jan. 11, 2026. [Online]. Available: https://nla.gov.au/nla.obj-234411506/view

[13] "Islam, N.U., Hussain, S.A., Abbas, S.Q. and Ashraf, M. (2010) Mineral Statistics of Pakistan. Geological Survey of Pakistan, Special Issue. - References - Scientific Research Publishing." Accessed: Jan. 11, 2026. [Online]. Available: https://www.scirp.org/reference/referencespapers?referenceid=2805698

[14] "Jan, M.Q. and Gauhar, S.H. (2013) Earth Sciences and Mineral Exploration History of Pakistan with Reference to Khyber Pakhtunkhwa and Its Adjacent Tribal Areas. Abstract Volume, Sustainable Utilization of Natural Resources of the Khyber Pakhtunkhwa and" Accessed: Jan. 11, 2026. [Online]. Available: https://www.scirp.org/%28S%28mllvtr455ztxky45opcgzyis%29%29/reference/referencespapers?referenceid=2791351

[15] H. M. Rajesh, "Application of remote sensing and GIS in mineral: Resource mapping - An

overview," *J. Mineral. Petrol. Sci.*, vol. 99, no. 3, 2024, [Online]. Available: https://www.researchgate.net/publication/45363148_Application_of_remote_sensing_and_GIS_in_mineral_Resource_mapping_-_An_overview

[16] R. Rajan Girija and S. Mayappan, "Mapping of mineral resources and lithological units: a review of remote sensing techniques," *Int. J. Image Data Fusion*, vol. 10, no. 2, pp. 79–106, Apr. 2019, doi: 10.1080/19479832.2019.1589585.

[17] M. H. Amin B. Pour, "Detection of hydrothermal alteration zones in a tropical region using satellite remote sensing data: Bau goldfield, Sarawak, Malaysia," *Ore Geol. Rev.*, vol. 54, 2013, [Online]. Available: https://www.researchgate.net/publication/236179595_Detection_of_hydrothermal_alteration_zones_in_a_tropical_region_using_satellite_remote_sensing_data_Bau_goldfield_Sarawak_Malaysia

[18] Seyed Mohammad Bolouki, Hamid Reza Ramazi, Amin Beiranvand Pour, "A Remote Sensing-Based Application of Bayesian Networks for Epithermal Gold Potential Mapping in Ahar-Arasbaran Area, NW Iran," *Remote Sens*, vol. 12, no. 1, p. 105, 2020, doi: https://doi.org/10.3390/rs12010105.

[19] Mamadou Traore, Jonas Didero Takodjou Wambo, "Lithological and alteration mineral mapping for alluvial gold exploration in the south east of Birao area, Central African Republic using Landsat-8 Operational Land Imager (OLI) data," *J. African Earth Sci.*, vol. 170, p. 103933, 2020, [Online]. Available: https://www.sciencedirect.com/science/article/abs/pii/S1464343X20301849

[20] F. D. Amr Abd El-Raouf, "Utilizing Remote Sensing and Satellite-Based Bouguer Gravity data to Predict Potential Sites of Hydrothermal Minerals and Gold Deposits in Central Saudi Arabia," *Minerals*, vol. 13, no. 8, p. 1092, 2023, doi: https://doi.org/10.3390/min13081092.

[21] Y. L. Chuntao Yin, "Mapping Ni-Cu-Platinum Group Element-Hosting, Small-Sized, Mafic-Ultramafic Rocks Using WorldView-3 Images and a Spatial-Spectral Transformer Deep Learning Method," *Econ. Geol.*, vol. 119, no. 3, pp. 665–680, 2024, [Online]. Available: https://pubs.geoscienceworld.org/segweb/economicgeology/article/119/3/665/634488/Mapping-Ni-Cu-Platinum-Group-Element-Hosting-Small

[22] Amin Beiranvand Pour, Yongcheol Park, "Mapping Listvenite Occurrences in the Damage Zones of Northern Victoria Land, Antarctica Using ASTER Satellite Remote Sensing Data," *Remote Sens*, vol. 11, no. 2, p. 1408, 2019, [Online]. Available: https://www.mdpi.com/2072-4292/11/12/1408

[23] L. L. Nazir Ul Islam, "Mapping Alteration Zones for Detection of Economic Minerals using Integrated Tools in District Lower Dir, Northwest Khyber Pakhtunkhwa, Pakistan," *Int. J. Econ. Environ. Geol.*, vol. 14, no. 2, 2023, [Online]. Available: https://www.econ-environ-geol.org/index.php/ojs/article/view/135

[24] J. C. Guanyun Zhou, "Three-dimensional mineral prospectivity mapping based on natural language processing and random forests: A case study of the Xiyu diamond deposit, China," *Ore Geol. Rev.*, vol. 169, p. 106082, 2024, [Online]. Available: https://www.sciencedirect.com/science/article/pii/S0169136824002154

[25] A. E. M. Reda Amer, "ASTER spectral analysis for alteration minerals associated with gold mineralization," *Ore Geol. Rev.*, vol. 75, pp. 239–251, 2016, [Online]. Available: https://www.sciencedirect.com/science/article/abs/pii/S0169136815302675

[26] Z. M. Martin Flower, "Project targets mantle dynamics and Tethyan Hazard mitigation," *Eos Trans. Am. Geophys. Union*, vol. 81, no. 49, 2000.

[27] "Lithologic mapping in arid regions with Landsat Thematic Mapper data: Meatiq Dome, Egypt." Accessed: Jan. 11, 2026.

[28] R. B. R. Hébert, "The Indus–Yarlung Zangbo ophiolites from Nanga Parbat to Namche Barwa syntaxes, southern Tibet: First synthesis of petrology, geochemistry, and geochronology with incidences on geodynamic reconstructions of Neo-Tethys," *Gondwana*

Res., vol. 22, no. 2, pp. 377–397, 2012, [Online]. Available: https://www.sciencedirect.com/science/article/abs/pii/S1342937X11002838

[29] Y. Ninomiya, "Mapping quartz, carbonate minerals, and mafic-ultramafic rocks using remotely sensed multispectral thermal infrared ASTER data</title>," *Thermosense XXIV*, vol. 4710, pp. 191–202, Mar. 2002, doi: 10.1117/12.459566.

[30] K. M. Shuhab D. Khan, "Mapping of Muslim Bagh ophiolite complex (Pakistan) using new remote sensing, and field data," *J. Asian Earth Sci.*, vol. 30, no. 2, pp. 333–343, 20073, [Online]. Available: https://www.sciencedirect.com/science/article/abs/pii/S1367912006002768

[31] M. E. Brian E. Tucker, "Issues in Urban Earthquake Risk," *Issues Urban Earthq. Risk*, 1994, doi: 10.1007/978-94-015-8338-1.

[32] "Petrology of the mantle rocks from the Muslim Bagh Ophiolite, Balochistan, Pakistan." Accessed: Jan. 11, 2026. [Online]. Available: https://www.researchgate.net/publication/269628837_Petrology_of_the_mantle_rocks_from_the_Muslim_Bagh_Ophiolite_Balochistan_Pakistan

[33] "Bilgrami, S.A. (1956) Mineralogy and Petrology of Muslimbagh Igneous Complex. Ph.D. Thesis, University of Manchester, UK. - References - Scientific Research Publishing." Accessed: Jan. 11, 2026. [Online]. Available: https://www.scirp.org/reference/referencespapers?referenceid=2791485

[34] S. A BILGRAMI, "Distribution of Cu, Ni, Co, V, and Cr in Rocks of the Hindubagh Igneous Complex, Zhob Valley, West Pakistan ," GSA Bulletin. Accessed: Jan. 11, 2026. [Online]. Available: https://pubs.geoscienceworld.org/gsa/gsabulletin/article-abstract/72/12/1729/5279/Distribution-of-Cu-Ni-Co-V-and-Cr-in-Rocks-of-the?redirectedFrom=fulltext

[35] Raymond H. Nagell, "Sulfur, fluorspar, magnesite, and aluminous chromite in Pakistan," *Open-File Rep.*, 1975, [Online]. Available: https://pubs.usgs.gov/publication/ofr75496

[36] Asrarullah, "Chromite and mining in Pakistan," *Geogr. Rec*, vol. 16, pp. 1–13, 1961.

[37] "Mineralogical mapping in the Cuprite Mining District, Nevada." Accessed: Jan. 11, 2026. [Online].Available:https://www.researchgate.net/publication/24323153_Mineralogical_mapping_in_the_Cuprite_Mining_District_Nevada

[38] Fred A. Kruse, "Use of airborne imaging spectrometer data to map minerals associated with hydrothermally altered rocks in the northern grapevine mountains, Nevada, and California," *Remote Sens. Environ.*, vol. 24, no. 1, pp. 31–51, 1988, [Online]. Available: https://www.sciencedirect.com/science/article/abs/pii/0034425788900041

[39] L. L. Waqar Ahmad, "Lithological Classification Using ZY1-02D Hyperspectral Data by Means of Machine Learning and Deep Learning Methods in the Kohat–Pothohar Plateau, Khyber Pakhtunkhwa, Pakistan," *Remote Sens.*, vol. 17, no. 8, p. 1356, 2025, doi: https://doi.org/10.3390/rs17081356.

[40] X. S. Li Chen, "Mapping Alteration Minerals Using ZY-1 02D Hyperspectral Remote Sensing Data in Coalbed Methane Enrichment Areas," *Remote Sens.*, vol. 15, no. 14, p. 3590, 2023, [Online]. Available: https://www.mdpi.com/2072-4292/15/14/3590

[41] T. C. Muhammad Ahsan Mahboob, "Predictive modelling of mineral prospectivity using satellite remote sensing and machine learning algorithms," *Remote Sens. Appl. Soc. Environ.*, vol. 36, p. 101316, 2024, [Online]. Available: https://www.sciencedirect.com/science/article/pii/S2352938524001800

[42] M. W. Nazir Jan, Nasru Minallah, Madiha Sher, "Advanced Mineral Deposit Mapping via Deep Learning and SVM Integration With Remote Sensing Imaging Data," *Eng. Reports*, 2024, [Online]. Available: https://onlinelibrary.wiley.com/doi/full/10.1002/eng2.13031

[43] Muhammad Anees, Muaaz Shoukat, "Integration of Multi and Hyperspectral Satellite Data for Identification of Potentially Mineralized Zones in the Southern Metamorphic Belt of Chitral (NW Pakistan)," *J. Sp. Technol.*, vol. 22, no. 1, pp. 57–69, 2022,

[44] E. G. Agustin Lobo, "Machine Learning for Mineral Identification and Ore Estimation

from Hyperspectral Imagery in Tin–Tungsten Deposits: Simulation under Indoor Conditions," *Remote Sens*, vol. 13, no. 16, p. 3258, 2021, [Online]. Available: https://www.mdpi.com/2072-4292/13/16/3258

[45] H. S. K. Muhammad Jaleed Khan, "Modern Trends in Hyperspectral Image Analysis: A Review," *IEEE Access*, 2018, [Online]. Available: https://ieeexplore.ieee.org/document/8314827

[46] R. N. Giri, R. R. Janghel, H. Govil, and G. Mishra, "A stacked ensemble learning-based framework for mineral mapping using AVIRIS-NG hyperspectral image," *J. Earth Syst. Sci. 2024 1332*, vol. 133, no. 2, pp. 107-, May 2024, doi: 10.1007/S12040-024-02317-Z.

[47] N. U. Islam *et al.*, "Mineralogical mapping and lithological discrimination by using ASTER remote sensing data in the Chitral region, Khyber Pakhtunkhwa, Northern Pakistan," *Earth Sci. Informatics 2024 176*, vol. 17, no. 6, pp. 6075–6094, Oct. 2024, doi: 10.1007/S12145-024-01483-4.

[48] "Extracting lithologic information from ASTER multispectral thermal infrared data in the northeastern Pamirs." Accessed: Jan. 11, 2026. [Online]. Available: https://www.researchgate.net/publication/281162879_Extracting_lithologic_information_from_ASTER_multispectral_thermal_infrared_data_in_the_northeastern_Pamirs

[49] Enton Bedini, "The use of hyperspectral remote sensing for mineral exploration: a review," *J. Hyperspectral Remote Sens.*, vol. 7, no. 4, p. 189, 2017, [Online]. Available: https://www.researchgate.net/publication/363465665_The_use_of_hyperspectral_remote_sensing_for_mineral_exploration_a_review

[50] "Small & Medium Enterprise Development Authority, Government of Pakistan Report on Killa Saifullah District Profile," *Gov. Pakistan, Islam.*, 2004, [Online]. Available: https://smeda.org/phocadownload/Balochistan/killa_saifullah_profile.pdf

[51] D. D. P. 2021 Government of Baluchistan, "UNICEF and Planning & Development Department," *Kill. Saifullah, UNICEF, Quetta*, 2021, [Online]. Available: https://www.unicef.org/pakistan/media/2966/file/Profiles of Underserved Areas of Quetta City of Balochistan, Pakistan.pdf

[52] P. Molnar and P. Tapponnier, "Cenozoic tectonics of Asia: Effects of a continental collision," *Science (80-.).*, vol. 189, no. 4201, pp. 419–426, 1975, doi: 10.1126/SCIENCE.189.4201.419.

[53] "Vredenburg, E. (1901) A Geological Sketch of Balochistan Desert and Part of Eastern Persia. Geological Survey of India, Memoir, 31, 179-302. - References - Scientific Research Publishing." Accessed: Jan. 11, 2026. [Online]. Available: https://www.scirp.org/reference/referencespapers?referenceid=2791434

[54] Dilek and Yildirim, "Penrose Conference on "Ophiolites and Oceanic Crust: New Insights from Field Studies and Ocean Drilling Program," *nsf*, vol. 98, no. 9813451, p. 13451, 1998, Accessed: Jan. 11, 2026. [Online]. Available: https://ui.adsabs.harvard.edu/abs/1998nsf....9813451D/abstract

[55] Z. A. E. M. Moores, D. H. Roeder, S. G. Abbas, "Geology and emplacement of the Muslim Bagh ophiolite complex," *A. Panayiotou (Ed.), Ophiolites Symp. Geol. Surv. Dep. Cyprus*, pp. 424–429, 1980.

[56] F. B. Khalid Mahmood, "40Ar/39Ar dating of the emplacement of the Muslim Bagh ophiolite, Pakistan," *Tectonophysics*, vol. 220, no. 1–3, pp. 169–181, 1995, [Online]. Available: https://www.sciencedirect.com/science/article/abs/pii/0040195195000175

[57] A. N. K. Benn, "Mantle—crust transition zone and origin of wehrlitic magmas: Evidence from the Oman ophiolite," *Tectonophysics*, vol. 151, no. 1–4, pp. 75–85, 1988, [Online]. Available: https://www.sciencedirect.com/science/article/abs/pii/0040195188902417

[58] F. Boudier and A. Nicolas, "Nature of the moho transition zone in the Oman ophiolite," *J. Petrol.*, vol. 36, no. 3, pp. 777–796, Jun. 1995, doi: 10.1093/PETROLOGY/36.3.777.

[59] J. A. Richards and X. Jia, "Remote sensing digital image analysis: An introduction," *Remote Sens. Digit. Image Anal. An Introd.*, pp. 1–439, 2006, doi: 10.1007/3-540-29711-1.

[60] "SWIR - ASTER User Advisory." Accessed: Jan. 11, 2026. [Online]. Available: https://asterweb.jpl.nasa.gov/swir-alert.asp

[61] J. R. Jensen and K. Lulla, "Introductory digital image processing: A remote sensing perspective," *Geocarto Int.*, vol. 2, no. 1, p. 65, 1987, doi: 10.1080/10106048709354084;CSUBTYPE:STRING:SPECIAL;PAGE:STRING:ARTICLE/CHAPTER.

[62] A. Shaban, "Fundamentals of Satellite Remote Sensing," *Springer Water*, pp. 1–14, 2022, doi: 10.1007/978-3-031-15549-9_1.

[63] C. E. W. Conghe Song, "Classification and Change Detection Using Landsat TM Data: When and How to Correct Atmospheric Effects?," *Remote Sens. Environ.*, vol. 75, no. 2, pp. 230–244, 2001, [Online]. Available: https://www.sciencedirect.com/science/article/abs/pii/S0034425700001693

[64] T. Toutin, "Geometric processing of remote sensing images: Models, algorithms and methods," *Int. J. Remote Sens.*, vol. 25, no. 10, pp. 1893–1924, May 2004, doi: 10.1080/01431160310001016l1;PAGE:STRING:ARTICLE/CHAPTER.

[65] C. S. Fraser and H. B. Hanley, "Bias compensation in rational functions for Ikonos satellite imagery," *Photogramm. Eng. Remote Sensing*, vol. 69, no. 1, pp. 53–57, Jan. 2003, doi: 10.14358/PERS.69.1.53.

[66] B. L. M. Gyanesh Chander, "Summary of current radiometric calibration coefficients for Landsat MSS, TM, ETM+, and EO-1 ALI sensors," *Remote Sens. Environ.*, vol. 113, no. 5, pp. 893–903, 2009, [Online]. Available: https://www.sciencedirect.com/science/article/abs/pii/S0034425709000169

[67] N. Z. E. S. Eric F. Vermote, "Atmospheric correction of MODIS data in the visible to middle infrared: first results," *Remote Sens. Environ.*, vol. 83, no. 1–2, pp. 97–111, 2002, [Online]. Available: https://www.sciencedirect.com/science/article/abs/pii/S0034425702000895

[68] K. J. Thome, S. F. Biggar, and P. N. Slater, "Effects of assumed solar spectral irradiance on intercomparisons of Earth-observing sensors," *Sensors, Syst. Next-Generation Satell. V*, vol. 4540, p. 260, Dec. 2001, doi: 10.1117/12.450668.

[69] E. F. Vermote, D. Tanré, J. L. Deuzé, M. Herman, and J. J. Morcrette, "Second simulation of the satellite signal in the solar spectrum, 6s: an overview," *IEEE Trans. Geosci. Remote Sens.*, vol. 35, no. 3, pp. 675–686, 1997, doi: 10.1109/36.581987.

[70] Y. J. Kaufman and C. Sendra, "Algorithm for automatic atmospheric corrections to visible and near-ir satellite imagery," *Int. J. Remote Sens.*, vol. 9, no. 8, pp. 1357–1381, 1988, doi: 10.1080/01431168808954942.

[71] R. S. Fraser and Y. J. Kaufman, "The Relative Importance of Aerosol Scattering and Absorption in Remote Sensing," *IEEE Trans. Geosci. Remote Sens.*, vol. GE-23, no. 5, pp. 625–633, 1985, doi: 10.1109/TGRS.1985.289380.

[72] R. Richter and D. Schläpfer, "Geo-atmospheric processing of airborne imaging spectrometry data. Part 2: Atmospheric/topographic correction," *Int. J. Remote Sens.*, vol. 23, no. 13, pp. 2631–2649, Jul. 2002, doi: 10.1080/01431160110115834.

[73] L. S. Bernstein *et al.*, "A new method for atmospheric correction and aerosol optical property retrieval for VIS-SWIR multi- and hyperspectral imaging sensors: QUAC (QUick Atmospheric Correction)," *Int. Geosci. Remote Sens. Symp.*, vol. 5, pp. 3549–3552, 2005, doi: 10.1109/IGARSS.2005.1526613.

[74] L. S. Bernstein, "Quick atmospheric correction code: algorithm description and recent upgrades," *Opt. Eng.*, vol. 51, no. 11, p. 111719, Jul. 2012, doi: 10.1117/1.OE.51.11.111719.

[75] S. M. Adler-Golden *et al.*, "Atmospheric correction for shortwave spectral imagery based on MODTRAN4</title>," *Imaging Spectrom. V*, vol. 3753, pp. 61–69, Oct. 1999, doi: 10.1117/12.366315.

[76] M. W. Matthew *et al.*, "Atmospheric correction of spectral imagery: Evaluation of the FLAASH algorithm with AVIRIS data," *Proc. - Appl. Imag. Pattern Recognit. Work.*, vol. 2002-

January, pp. 157–163, 2002, doi: 10.1109/AIPR.2002.1182270.

[77] M. L. E. Robert O. Green, "Imaging Spectroscopy and the Airborne Visible/Infrared Imaging Spectrometer (AVIRIS)," *Remote Sens. Environ.*, vol. 65, no. 3, pp. 227–248, 1998, [Online]. Available: https://www.sciencedirect.com/science/article/abs/pii/S0034425798000649

[78] R. N. Clark, T. V. V. King, M. Klejwa, G. A. Swayze, and N. Vergo, "High spectral resolution reflectance spectroscopy of minerals," *J. Geophys. Res.*, vol. 95, no. B8, pp. 12653–12680, Aug. 1990, doi: 10.1029/JB095IB08P12653;WGROUP:STRING:PUBLICATION.

[79] F. A. Kruse, A. B. Lefkoff, "The spectral image processing system (SIPS)—interactive visualization and analysis of imaging spectrometer data," *Remote Sens. Environ.*, vol. 44, no. 2–3, pp. 145–163, 1993, [Online]. Available: https://www.sciencedirect.com/science/article/abs/pii/003442579390013N

[80] F. A. K. Joseph W. Boardman, "Mapping target signatures via partial unmixing of AVIRIS data," *Summ. Fifth Annu. JPL Airborne Earth Sci. Work. Vol. 1 AVIRIS Work.*, 1995, [Online]. Available: https://ntrs.nasa.gov/citations/19950027316

[81] J. M. P. Nascimento and J. M. B. Dias, "Vertex component analysis: A fast algorithm to unmix hyperspectral data," *IEEE Trans. Geosci. Remote Sens.*, vol. 43, no. 4, pp. 898–910, Apr. 2005, doi: 10.1109/TGRS.2005.844293.

[82] M. E. Winter, "N-FINDR: an algorithm for fast autonomous spectral end-member determination in hyperspectral data," *https://doi.org/10.1117/12.366289*, vol. 3753, pp. 266–275, Oct. 1999, doi: 10.1117/12.366289.

[83] A. Plaza, P. Martínez, R. Pérez, and J. Plaza, "A quantitative and comparative analysis of endmember extraction algorithms from hyperspectral data," *IEEE Trans. Geosci. Remote Sens.*, vol. 42, no. 3, pp. 650–663, Mar. 2004, doi: 10.1109/TGRS.2003.820314.

[84] A. A. Green, M. Berman, P. Switzer, and M. D. Craig, "A Transformation for Ordering Multispectral Data in Terms of Image Quality with Implications for Noise Removal," *IEEE Trans. Geosci. Remote Sens.*, vol. 26, no. 1, pp. 65–74, 1988, doi: 10.1109/36.3001.

[85] Joseph W. Boardman, "Automating spectral unmixing of AVIRIS data using convex geometry concepts," *JPL, Summ. 4th Annu. JPL Airborne Geosci. Work. Vol. 1 AVIRIS Work.*, 1993, [Online]. Available: https://ntrs.nasa.gov/citations/19950017428

[86] G. A. Licciardi and F. Del Frate, "Pixel unmixing in hyperspectral data by means of neural networks," *IEEE Trans. Geosci. Remote Sens.*, vol. 49, no. 11 PART 1, pp. 4163–4172, Nov. 2011, doi: 10.1109/TGRS.2011.2160950.

[87] Boardman J W, "Automated spectral analysis: a geological example using AVIRIS data, north Grapevine Mountains, Nevada," *Proc. 10th Themat. Conf. Geol. Remote Sens.*, 1994, [Online]. Available: https://jglobal.jst.go.jp/en/detail?JGLOBAL_ID=200902187647539097

[88] C. I. Chang and A. Plaza, "A fast iterative algorithm for implementation of pixel purity index," *IEEE Geosci. Remote Sens. Lett.*, vol. 3, no. 1, pp. 63–67, Jan. 2006, doi: 10.1109/LGRS.2005.856701.

[89] C. I. Chang, "Hyperspectral Data Processing: Algorithm Design and Analysis," *Hyperspectral Data Process. Algorithm Des. Anal.*, Mar. 2013, doi: 10.1002/9781118269787.

[90] J. B. Adams, M. O. Smith, and P. E. Johnson, "Spectral mixture modeling: A new analysis of rock and soil types at the Viking Lander 1 Site," *J. Geophys. Res. Solid Earth*, vol. 91, no. B8, pp. 8098–8112, Jul. 1986, doi: 10.1029/JB091IB08P08098.

[91] G. R. Hunt, "Spectral signatures of particulate minerals in the visible and near infrared," *Geophysics*, vol. 42, no. 3, pp. 501–513, Apr. 1977, doi: 10.1190/1.1440721.

[92] R. N. Clark, "Spectroscopy of rocks and minerals and principles of spectroscopy," 1999.

[93] R. N. Clark and T. L. Roush, "Reflectance spectroscopy: quantitative analysis techniques for remote sensing applications.," *J. Geophys. Res.*, vol. 89, no. B7, pp. 6329–6340, Jul. 1984, doi: 10.1029/JB089IB07P06329;CTYPE:STRING:JOURNAL.

[94] Freek van der Meer, "Analysis of spectral absorption features in hyperspectral imagery," *Int. J. Appl. Earth Obs. Geoinf.*, vol. 5, no. 1, pp. 55–68, 2004, [Online]. Available: https://www.sciencedirect.com/science/article/abs/pii/S0303243403000382

[95] Hugh R. Rollinson, "Using Geochemical Data: Evaluation, Presentation, Interpretation - 1st," Routledge. Accessed: Jan. 11, 2026. [Online]. Available: https://www.routledge.com/Using-Geochemical-Data-Evaluation-Presentation-Interpretation/Rollinson/p/book/9780582067011

[96] A. Streckeisen, "To each plutonic rock its proper name," *Earth-Science Rev.*, vol. 12, no. 1, pp. 1–33, 1976, [Online]. Available: https://www.sciencedirect.com/science/article/abs/pii/0012825276900520

[97] Fred A. Kruse, "Mapping surface mineralogy using imaging spectrometry," *Geomorphology*, vol. 137, no. 1, pp. 41–56, 2012, [Online]. Available: https://www.sciencedirect.com/science/article/abs/pii/S0169555X11001516

[98] Floyd F Sabins, "Remote sensing for mineral exploration," *Ore Geol. Rev.*, vol. 14, no. 3–4, pp. 157–183, 1999, [Online]. Available: https://www.sciencedirect.com/science/article/abs/pii/S0169136899000074

[99] K. E. L. Roger N. Clark, Gregg A. Swayze, "Imaging spectroscopy: Earth and planetary remote sensing with the USGS Tetracorder and expert systems," *J. Geophys. Res. Planets*, 2003, [Online]. Available: https://agupubs.onlinelibrary.wiley.com/doi/10.1029/2002JE001847

[100] A. B. Pour and M. Hashim, "The application of ASTER remote sensing data to porphyry copper and epithermal gold deposits," *Ore Geol. Rev.*, vol. 44, pp. 1–9, Feb. 2012, doi: 10.1016/J.OREGEOREV.2011.09.009.

[101] H. M. A. van der W. Freek D. van der Meer, "Multi- and hyperspectral geologic remote sensing: A review," *Int. J. Appl. Earth Obs. Geoinf.*, vol. 14, no. 1, pp. 112–128, 2012, [Online].Available:https://www.sciencedirect.com/science/article/abs/pii/S0303243411001103

[102] S. L. Moritz Kirsch, "Integration of Terrestrial and Drone-Borne Hyperspectral and Photogrammetric Sensing Methods for Exploration Mapping and Mining Monitoring," *Remote Sens*, vol. 10, no. 9, p. 1366, 2018, [Online]. Available: https://www.mdpi.com/2072-4292/10/9/1366